ADVANCED MATERIALS TECHNOLOGIES
www.advmattechnol.de

Recent Advances in Tunable/Reconfigurable Terahertz Metadevices Based on Phase-Change Materials

*Bowen Li, Jiachi Liao, Di Yin, He Shao, Shuai Zhang, Baojie Chen, Chi Hou Chan, and Johnny C. Ho**

Emerging artificial intelligence and Internet of Things (IoT) technologies have greatly enhanced daily life, yet processing vast data volumes poses challenges for computing hardware and communication systems. Terahertz (THz) waves, positioned between microwaves and infrared light, offer significant potential for future communication and sensing applications due to their wide bandwidth, high data rate, superior resolution, and non-destructive capabilities. However, traditional passive THz devices face adaptive control and dynamic modulation limitations. The emergence of tunable and reconfigurable metadevices, especially those using phase-change materials, provides promising solutions through substantial and rapid modulation of electromagnetic responses. This review examines recent advancements in THz metadevices utilizing phase-transition materials, focusing on mechanisms like insulator-to-metal transitions, amorphous-to-crystal transformations, ferroelectric behavior, and liquid-crystal transitions. It summarizes strategies in structural design, material selection, and device fabrication. Furthermore, it discusses the latest developments in THz modulation and applications using phase-change metadevices, highlighting key performance parameters such as frequency range, modulation depth, tunability, and switching speed. Finally, the review outlines current challenges and future prospects in advancing adaptive THz metadevices, pointing to potential pathways for dynamic, multifunctional THz systems.

1. Introduction

Over the past decade, a surge of Internet of Things (IoT) technologies, powered by machine learning and neural network algorithms, has emerged and rapidly advanced. Innovations such as smart transportation systems, intelligent robotics, mobile wearables, and digital medical diagnostics have significantly improved daily living standards and industrial productivity worldwide by enhancing wireless connectivity capabilities.[1–5] However, the enormous data transmission and processing demands have strained conventional IoT sensing and communication hardware. This has created an urgent need for next-generation intelligent edge devices that offer high speed, high density, and low-power consumption. Terahertz (THz) waves, occupying the spectral region between microwaves and infrared light (0.1 to 10 THz), hold immense promise for various IoT applications, including high-frequency wireless communications, security surveillance, and biomedical diagnostics.[6–8] Their potential stems from unique features such as extensive bandwidth, high data transmission rate, superior non-destructive testing qualities, and advanced sensing mechanisms.[9–11] Despite these advantages, the inherent properties of THz waves—strong penetration and relatively weak photon energy—pose significant challenges for detection and modulation using standard passive optical components. This has impeded progress in developing diverse THz functional devices until the advent of tunable and reconfigurable metadevices (MDs).

MDs are metamaterial devices composed of periodic arrays of artificial microstructures with subwavelength dimensions, exhibiting unique characteristics within specific frequency bands, such as negative refraction, negative magnetic permeability, and the inverse Doppler effect.[12–14] Early demonstrations of generalized Snell's laws using V-shaped metallic nanoantennas established metasurfaces as lightweight, 2D alternatives to bulky optical components.[15,16] By designing MDs as resonant structures, they can strongly interact with THz photons and produce distinctive electromagnetic responses by altering their

B. Li, J. Liao, D. Yin, H. Shao, S. Zhang, J. C. Ho
Department of Materials Science and Engineering
City University of Hong Kong
Hong Kong, SAR 999077, China
E-mail: johnnyho@cityu.edu.hk
B. Li, J. C. Ho
Shenzhen Research Institute of City University of Hong Kong
Shenzhen 518057, China
C. H. Chan
Department of Electrical Engineering
City University of Hong Kong
Hong Kong, SAR 999077, China
B. Li, B. Chen, C. H. Chan, J. C. Ho
State Key Laboratory of Terahertz and Millimeter Waves
City University of Hong Kong
Hong Kong, SAR 999077, China

The ORCID identification number(s) for the author(s) of this article can be found under https://doi.org/10.1002/admt.202500935

DOI: 10.1002/admt.202500935

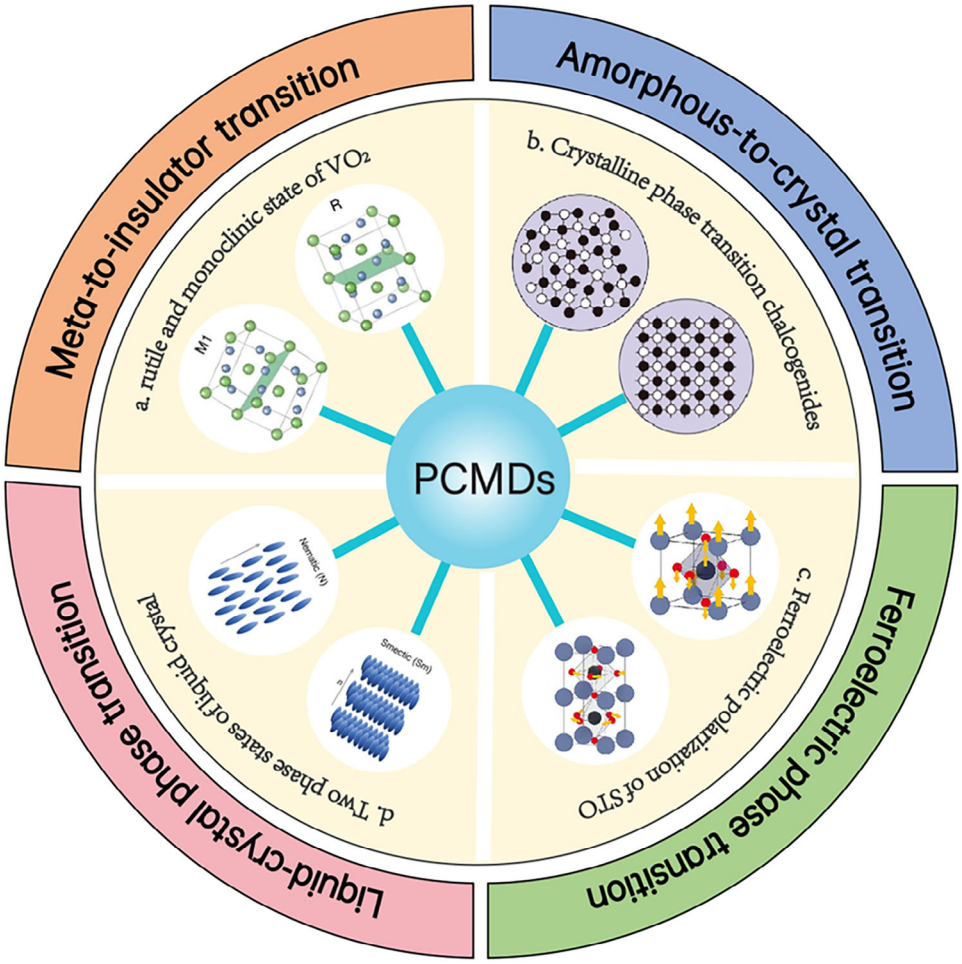

Figure 1. An overview of the mechanisms and crystal structures of mainstream PCMs in PCMDs.

structural and material parameters. Recent research has focused on developing innovative THz devices like sensors, modulators, switches, filters, and absorbers.[17–20] Incorporating magnetic materials into these structures enhances the interaction between electromagnetic waves and matter,[21] offering improved resolution and sensitivity for biosensing applications. However, traditional designs with static geometries and fixed material properties struggle to adapt to dynamic environments, limiting their practical utility.[22–24] This challenge has spurred the development of tunable and reconfigurable MDs,[25] utilizing materials like semiconductors, graphene,[26–32] and phase-change materials (PCMs),[33–37] which exhibit significant changes in optical and electrical properties under external stimuli. Furthermore, the development of micro-electromechanical systems (MEMS) technology has also provided a platform for micro-mechanical tunable MDs, which can be classified into two categories. One category changes the electromagnetic characteristics by mechanically adjusting the vertical or horizontal spacing between layers.[38,39] The other category alters the electromagnetic response of the metadevice by deforming flexible materials.[40,41] However, such mechanically tuned MDs are still constrained by the inherent speed limitations of mechanical switches and the high cost of micro-nano fabrication. Additionally, in 2022, Riccardo et al. summarized the developments in THz modulators based on metamaterials. They highlighted key applications in sensing, wireless communications, and quantum electronics that have significantly benefited from these advances.[42] At the same time, Shohreh et al. also reported a review on THz metastructures for noninvasive biomedical sensing and characterization in future health care.[43]

In this review, we present an in-depth analysis of tunable and reconfigurable phase-change metadevices (PCMDs), focusing on tuning theory, PCMs' physical properties, structural design, fabrication, and multifunctional applications. It begins with an overview of typical active metasurface structures and their tuning parameters and mechanisms, followed by a detailed discussion of primary PCMs used in tunable THz MDs. These materials are categorized into four main types based on phase transition mechanisms: insulator-to-metal (IMT), amorphous-to-crystal (ACPT), ferroelectric phase (FEPT), and liquid-crystal (LCPT) transitions, as shown in **Figure 1**a. The review systematically outlines the phase transition characteristics of PCMs and explores design, fabrication, and optimization strategies for tunable PCMDs, providing valuable insights for developing adaptive MDs. Furthermore, recent advancements in THz modulation and applications based on PCMDs are compared and summarized,

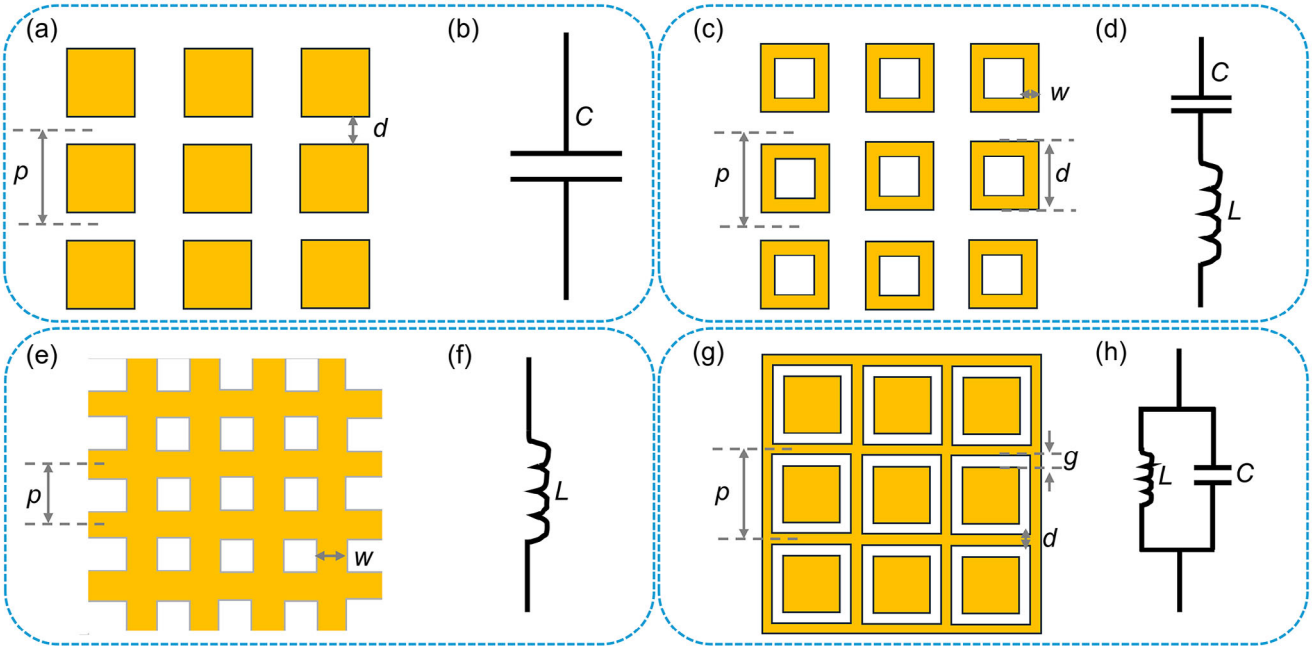

Figure 2. The theory of equivalent circuitry. a,b) Square patch array and its equivalent circuit.[45] c,d) Square ring array and its equivalent circuit with series connection of capacitance and inductance.[46] e,f) Square grid array and its equivalent circuit.[47] g,h) The square-ring gap array and its equivalent parallel capacitance and inductance circuit.[48]

considering factors like external stimuli, operating frequency, tunability, and switching speed. This comprehensive analysis offers practical guidance for developing tunable PCMDs. Finally, the review highlights current challenges and explores potential directions for evolving tunable and reconfigurable PCMDs.

2. Fundamental Theory

2.1. Equivalent Circuit Theory

Typically, the metasurface structure exhibits a resonant response upon the incidence of electromagnetic waves onto a metasurface device. If the unit structure size of the metasurface is considerably smaller than the wavelength of the incident wave, its resonant characteristics can be approximately analyzed using the equivalent circuit theory. This circuit description dates back several decades and is well developed in microwave frequency-selective surface (FSS).[44] The metasurface structure can be equivalently modeled as a series-parallel combination of resistors (R), inductors (L), and capacitors (C) in an electrical circuit. By calculating the values of R, L, and C, the resonant frequency of the metasurface structure can be determined, and the variation trend of the resonant frequency with changes in the device structural parameters can also be analyzed. Analyzing the operational mechanism of the device through the equivalent circuit method provides reverse guidance for the design of 2D metasurfaces. Below, the equivalent circuit theory is introduced by analyzing the metal patch and slot array structures.

As shown in **Figure** 2a, the metasurface consists of periodically arranged square metallic patches. Since most of the area within the unit cell is occupied by the patches, the self-inductance effect is significantly reduced and can be neglected. The gaps between adjacent periodic units become the dominant influencing factor during resonance. Upon normal incidence of electromagnetic waves, an induced electric field arises between the patch gaps along a direction parallel to the electric field, causing charge accumulation on both sides of the metal gaps. Consequently, the gaps between the patches can be equivalently modeled as capacitors. The metasurface primarily exhibits capacitive behavior, and its equivalent circuit is presented in Figure 2b. The capacitance value can be approximately calculated using the following formulas. For perpendicular incidence of transverse magnetic waves (TM), the equivalent capacitance is:[45]

$$C = \frac{2p\varepsilon_r}{\pi c Z_0}\left(1 - \frac{\sin^2\theta}{2\varepsilon_r}\right)\ln\left[\csc\left(\frac{\pi d}{2p}\right)\right] \quad (1)$$

For vertical incidence of transverse electric waves (TE), the equivalent capacitance is:

$$C = \frac{2p\varepsilon_r}{\pi c Z_0}\ln\left[\csc\left(\frac{\pi d}{2p}\right)\right] \quad (2)$$

where p denotes the period of the metasurface unit cell, d represents the spacing between adjacent metal patches, ϵ_r refers to the dielectric constant of the substrate, θ indicates the incident angle of the electromagnetic wave, and Z_0 corresponds to the characteristic impedance in free space.

The ring array is a fundamental building block for metadevice design, as shown in Figure 2c. Here, p denotes the period of the metasurface unit, w signifies the difference between the inner and outer widths of the square ring, d represents the outer side length of the square ring, and ϵ refers to the dielectric constant of the substrate. Moreover, the metal arms on both sides of the

square ring exhibit an inductive effect, while the gaps between adjacent rings demonstrate a capacitive effect. Consequently, the equivalent circuit of this structure comprises a series connection of inductance L and capacitance C, as depicted in Figure 2d. The corresponding expressions for calculating the equivalent inductance L and capacitance C are provided below:[46]

$$L = \frac{d}{\lambda} \ln\left[csc\frac{\pi}{p} + G\left(p, 2w, \lambda\right)\right] \tag{3}$$

$$C = 4\varepsilon_r \frac{d}{\lambda} \ln\left[csc\frac{\pi\left(p-d\right)}{2p} + G\left(p, p-d, \lambda\right)\right] \tag{4}$$

where μ denotes the wavelength of the incident wave and G represents the correction term.

The two aforementioned subwavelength structures possess complementary forms, as illustrated in Figure 2e. The complementary metasurface to the square patch array structure is a square grid-type structure, consisting of metal strips periodically arranged in horizontal and vertical directions in a crossed configuration. Upon external electromagnetic waves, the metasurface resonates, inducing currents in the metal strips, which can be treated as inductive elements. The grid gaps dominate the spatial distribution of the entire unit structure, making the capacitive effect negligible. Consequently, the square grid array structure can be effectively modeled as an independent inductance L, as depicted in Figure 2f. In this figure, p denotes the period of the metasurface unit, while w represents the widths of both the horizontal and vertical metal strips. When the electromagnetic wave is incident perpendicularly onto the surface of this device, the equivalent inductance L can be determined using the following equation:[47]

$$L = \frac{\mu_0 p}{2\pi} ln\left[csc\left(\frac{\pi w}{2p}\right)\right] \tag{5}$$

The square-ring slot array is a specific type of slot array structure, as illustrated in Figure 2g. In this metasurface configuration, the metal arms outside the rings on both sides along the direction of the incident electric field exhibit inductive behavior. In contrast, the slots between the metal arms and the square patches within the unit cell can be modeled as capacitive elements, as depicted in Figure 2h. The equivalent circuit for this structure consists of an inductor and a capacitor connected in parallel. In the figure, p denotes the period of the unit cell, g represents the width of the annular gap, and d indicates the width of the metal arm. At this stage, the expressions for calculating the equivalent inductance and capacitance in the circuit are provided as follows:[48]

$$L = \frac{p}{\lambda} ln\left[csc\frac{\pi d}{2p} + G\left(p, d, \lambda\right)\right] \tag{6}$$

$$C = 4\varepsilon_r \frac{d}{\lambda} \ln\left[csc\frac{\pi g}{2p} + G\left(p, g, \lambda\right)\right] \tag{7}$$

It should be noted that the derivation of the complementary structures herein is based on equivalent circuits. When aiming for more sophisticated metadevice designs, it is usually essential to incorporate the electromagnetic theory of diffraction and the Babinet principle.[49] For relevant details, please refer to previous reports. For example, Andreas et al. experimentally verified the complementarity of electric and magnetic fields as predicted by Babinet's principle.[50] Maksim et al. proposed a planar Babinet-inverted dimer metamaterial possessing strong optical activity.[51] These complementary design theories and manufacturing methods have great potential for exploitation in terahertz optics.

2.2. Tuning Mechanism in PCMDs

Typically, during the phase transition of PCMs, the reorganization of their energy band structures leads to the release of free charge carriers, thereby causing variations in the complex conductivity. As a result, these materials exhibit significant modulation depth in the THz band transmission. This phenomenon can be described using the Tinkham equation:[52,53]

$$\frac{\tilde{E}_{film+substrate}\left(\omega\right)}{\tilde{E}_{substrate}\left(\omega\right)} = \frac{1 + n_{substrate}}{1 + n_{substrate} + Z_0\tilde{\sigma}\left(\omega\right)d_{film}} \tag{8}$$

where Z_0 represents the impedance of free space, d_{film} denotes the thickness of the phase-change film, $\tilde{E}_{film+substrate}(\omega)$ refers to the transmission amplitude through the film and substrate, $\tilde{E}_{substrate}(\omega)$ represents the transmission amplitude through the substrate alone, and $n_{substrate}$ indicates the substrate's refractive index. For a phase-change film with constant thickness, assuming that the refractive index of the substrate remains nearly invariant within the studied frequency range, the ratio $|\frac{\tilde{E}_{film+substrate}(\omega)}{\tilde{E}_{substrate}(\omega)}|$ decreases as the conductivity of the film increases. Consequently, the modulation depth of the THz amplitude can be controlled by regulating the phase transition of PCMs.

In recent years, metasurface absorbers integrated with phase-change films have primarily utilized patterned phase-change films to replace the metallic patterns on the surface of conventional metamaterial absorbers, thereby enabling tunable/reconfigurable absorption of THz waves. The design of such tunable/reconfigurable metasurface absorbers is mainly guided by impedance matching, equivalent circuit modeling, and interference suppression. Conventional tunable THz absorbers typically consist of a three-layer structure: a periodic metal pattern on the top layer, a dielectric layer in the middle, and a continuous metallic reflective layer at the bottom.[54] Due to the presence of the continuous metallic layer at the bottom, the transmissivity of the metasurface absorber is generally negligible, and only the reflectivity is considered. The absorption characteristics of the metasurface can be calculated using an equivalent circuit model, where the periodic metal pattern can be approximated as a single R-L-C circuit. The equivalent impedance (Z_u) of this circuit can be expressed by the following equation:[55]

$$Z_u = R + j\omega L + \frac{1}{j\omega C} \tag{9}$$

where R, C, and L respectively represent the equivalent resistance, capacitance, and inductance of the periodic metal

pattern. For a dielectric layer with a ground plane, the equivalent impedance (Z_t) can be expressed as:[56]

$$Z_t = jZ_0\sqrt{\mu_r/\varepsilon_r}tan\left(\omega t\sqrt{\mu_0\varepsilon_0\mu_r\varepsilon_r}\right) \quad (10)$$

where Z_0 denotes the impedance of free space (377 Ω), μ_r and ϵ_r represent the relative permeability and permittivity of the dielectric layer. At the same time, μ_0 and ϵ_0 correspond to the magnetic permeability and permittivity of vacuum, ω signifies the angular frequency of the incident wave, and t indicates the thickness of the dielectric layer. Consequently, the input impedance (Z_{in}) of the absorber can be expressed as:

$$\frac{1}{Z_{in}} = \frac{1}{Z_u} + \frac{1}{Z_t} \quad (11)$$

Therefore, by controlling the phase transition of PCMs, their equivalent resistance, capacitance, inductance, dielectric constant, and magnetic permeability can be adjusted, thereby enabling the modulation of the absorption rate. Furthermore, designing various patterned metasurface structures can achieve the tunable characteristics of THz absorption rate, operating band, and absorption bandwidth, thus fulfilling the requirements of diverse application scenarios.[57] Additionally, to characterize the tunability and reconfigurability of PCMDs, the criterion of relative tuning range (W_{RTR}) has been proposed. This metric can be quantitatively evaluated using the following equation:[58,59]

$$W_{RTR} = \frac{(f_{max} - f_{min})}{f_{center}} = \frac{2(f_{max} - f_{min})}{(f_{max} + f_{min})} \quad (12)$$

where f_{max}, f_{min}, and f_{center} respectively denote the maximum, minimum, and center frequencies corresponding to a −10 dB reflection or 90% absorption rate. W_{RTR} quantifies the capability of PCMDs to vary their operating frequencies, with a larger value indicating wide-range tunability.[60]

Guided by the aforementioned tuning mechanisms, detailed tuning approaches based on phase-change material selection, periodic pattern design, dielectric spacer optimization, and thermal management will be elaborated upon in the following three sections to achieve tunable and reconfigurable PCMDs.

3. Physical Properties of Phase-Change Materials for MDs

3.1. Vanadium Dioxide (VO_2)

This type of Mott material represents a classic example of a strongly correlated oxide that experiences a first-order IMPT near 340 K, as identified by Morin in 1959. This transition is marked by sudden alterations in electrical, optical, and structural characteristics.[61] At high temperatures (T > 340 K), VO_2 exhibits a tetragonal rutile structure (space group $P4_2/mnm$) with lattice constants a = b ≈ 4.554 Å and c ≈ 2.851 Å. In this configuration, vanadium atoms are arranged linearly along the [001] crystallographic direction, forming continuous V—V chains with consistent V—V bond lengths of ≈2.85 Å.[62] The metallic conductivity originates from the delocalized d-orbital electrons (d_1|| orbitals) along these chains, contributing to a half-filled conduction band. When cooled below the critical temperature (T < 340 K), VO_2 shifts to a monoclinic insulating phase (space group $P2_1/c$) through a coupled structural and electronic reorganization. This phase is defined by lattice parameters a ≈ 5.752 Å, b ≈ 4.538 Å, c ≈ 5.382 Å, and a monoclinic angle $\beta \approx 122.6°$.[63] During this phase, the V—V chains experience dimerization, neighboring vanadium atoms form V—V dimers with alternating short (2.65 Å) and long (3.12 Å) bond lengths, disrupting translational symmetry in **Figure 3a**.[64] Simultaneously, the oxygen octahedra surrounding the vanadium atoms display tilting and twisting distortions, which decrease crystal symmetry and alter the electronic environment. These structural modifications lead to electron localization and create a bandgap of approximately 0.6 eV, as verified by photoemission spectroscopy and optical absorption studies (Figure 3b).[65]

The IMPT mechanism arises from the cooperative interaction between structural lattice distortions and correlated electronic effects. A Peierls-like instability, marked by V—V dimerization coupled with octahedral distortions, induces symmetry-breaking phase transitions that reduce thermodynamic free energy through systematic reorganization of orbital hybridization patterns as illustrated in Figure 3c. Simultaneously, in the insulating state, Mott-Hubbard correlations govern electronic behavior, where strong Coulomb repulsion among localized d-electrons enforces charge localization, stabilizing the insulating phase via Coulomb blockade phenomena.[66] The transition also involves dynamic phonon-electron coupling; for example, the A_g phonon mode at 192 cm^{-1} exhibits softening near the critical temperature, facilitating ultrafast structural switching on nanosecond timescales. Experimentally, as shown in Figure 3d,e and X-ray diffraction (XRD) patterns of VO_2/mica heterostructures display distinct (020) Bragg reflections at 39.8° for the monoclinic phase (M-VO_2), along with mica's (00l) peaks, confirming epitaxial growth without impurities or misalignment. Raman spectroscopy further identifies characteristic A_g modes (192, 223, 308, 389, 498 cm^{-1}) and B_g modes (264, 338 cm^{-1}) in the monoclinic phase, while the A_{1g} mode at 613 cm^{-1}, attributed to symmetric V—O stretching vibrations, provides a sensitive probe of octahedral distortions during phase transitions. VO_2's reversible and ultrafast response makes it highly promising for applications such as thermochromic smart windows, ultrafast optical switches, and neuromorphic computing devices. However, practical implementation demands precise control over crystal quality and strain engineering to optimize switching efficiency and cyclability. Advanced synthesis methods, such as pulsed laser deposition (PLD) and molecular beam epitaxy (MBE), are essential for designing VO_2 thin films with tailored phase-transition properties.

In **Figure 4a**, both configurations display similar optical absorption patterns, with a prominent peak centered around 0.8 eV. This characteristic originates from electronic transitions between filled and empty bands, as confirmed by the alignment of this energy range with experimentally observed resonances in the dielectric response at ≈1.0 eV. The slight difference (0.2 eV) between predicted and measured peak positions may stem from many-body effects or interfacial polarization phenomena not

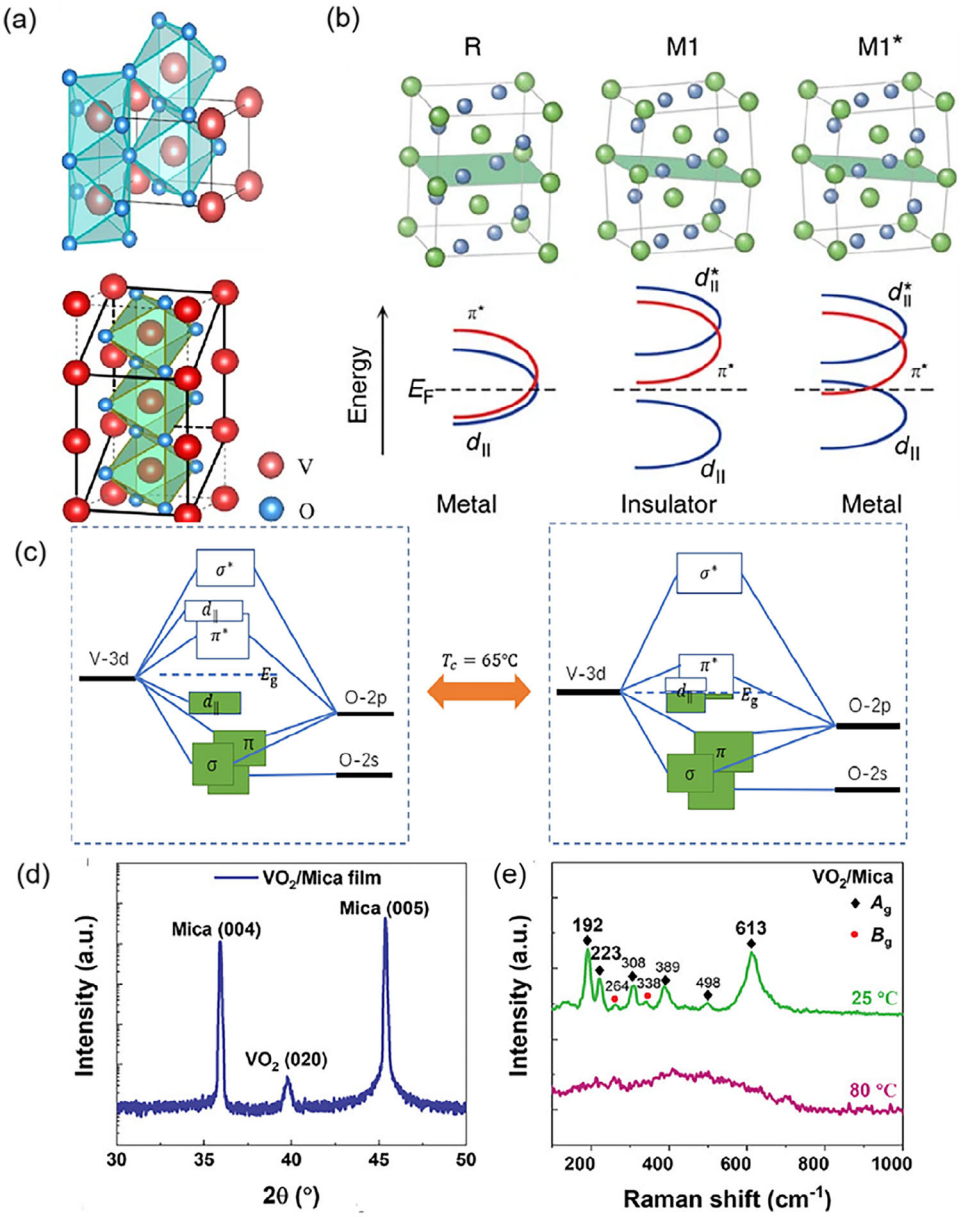

Figure 3. Schematic structure characterization and phase transition mechanism of VO_2. a) The rutile and monoclinic state of VO_2. Adapted with permission from.[64] Copyright 2024, Elsevier. b) Three different band structures of different phases. Adapted with permission from.[65] Copyright 2017, Nature Publishing Group. c) Dynamic changes of the VO_2 band structure. Adapted with permission from.[64] Copyright 2024, Elsevier. d) The XRD pattern of VO_2 growth on mica. e) Raman studies of the epitaxial VO_2 film at different temperatures. Adapted with permission from.[66] Copyright 2024, Wiley.

entirely captured in the computational model.[67] Furthermore, as shown in Figure 4b, rutile-phase VO_2 demonstrates higher optical reflectivity than its monoclinic counterpart, indicating enhanced photon reflection efficiency. This aligns with the metallic nature of the rutile phase, which facilitates stronger interactions with incident electromagnetic waves, as reflected in the improved reflectance spectrum. Indeed, the phase transition in VO_2 is associated with latent heat due to its thermal characteristics, offering potential applications in thermal management systems.[68] The material's capacity for reversible phase changes allows it to absorb or release heat during transitions, making it valuable for thermal regulation and energy storage technologies. Additionally, the phase transition induces variations in specific heat capacity and thermal conductivity, which are essential for designing devices requiring accurate thermal control.

Moreover, VO_2 is renowned for its remarkable phase transition properties, profoundly impacting its electrical, optical, and thermal characteristics. The phase transition from an insulating to a metallic state occurs around 68 °C, inducing substantial alterations in these properties (Figure 4c,d).[69] During this transformation, VO_2 exhibits a significant shift in electrical conductivity. In its insulating phase, VO_2 displays low conductivity like semiconductors. Conversely, upon transitioning into the metallic phase, its conductivity rises dramatically by several orders of

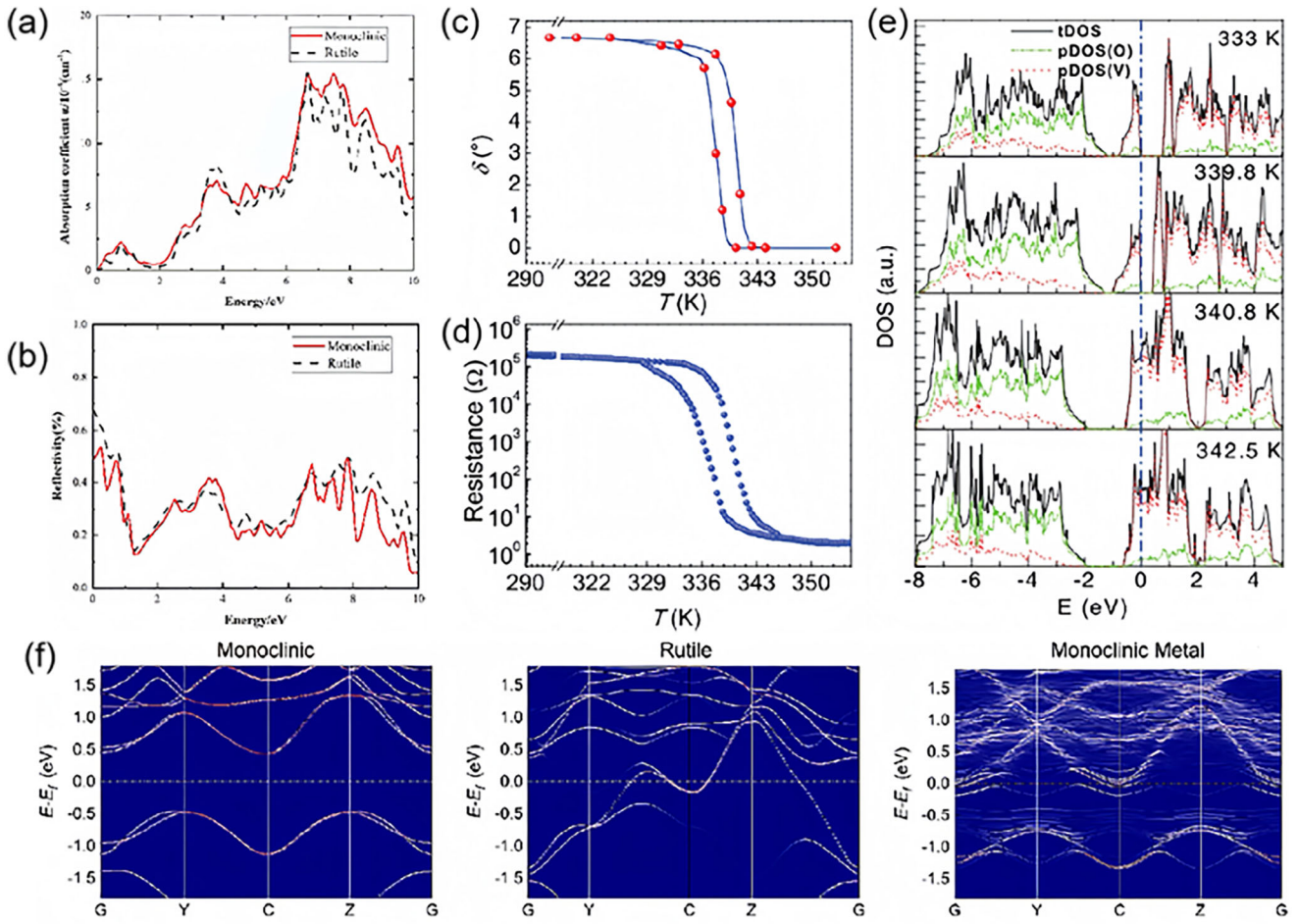

Figure 4. The phase transition properties and band structures of VO_2. a,b) The absorption coefficient and reflectivity of Monoclinic and Rutile states, respectively. Adapted permission with.[64] Copyright 2024, Elsevier. c,d) In situ comparison of V–V chain properties with temperature change. e) The temperature-dependent electronic density of states for metastable VO_2 phases was obtained through first-principles DFT simulations incorporating lattice thermal excitations. Adapted permission with.[70] Copyright 2010, American Physical Society. f) The band structures of different states of VO_2. Adapted permission with.[71] Copyright 2025, Nature Publishing Group.

magnitude. This sudden change stems from reconfiguring electron orbitals, facilitating electron delocalization in the metallic state. As depicted in Figure 4f, after transitioning from the Monoclinic structure to the Rutile structure, the energy band structure of VO_2 shows an overlap between the conduction and valence bands, validating its metallic nature. This capability to toggle between phases renders VO_2 highly appealing for applications in intelligent THz devices. Overall, the distinctive integration of electrical, optical, and thermal properties in VO_2, driven by its phase transition, enables a wide range of applications in electronics, optics, and energy domains. Yao et al.[64] explored the temperature-dependent electronic density in Figure 4e.

Continued research into enhancing these properties and elucidating their underlying mechanisms further expands the potential applications of VO_2-based materials. However, different synthesis methodologies for VO_2 inherently involve trade-offs. For example, achieving high film crystallinity often compromises uniformity control and process energy efficiency; conversely, cost-effective and scalable growth techniques frequently suffer from issues such as impurity incorporation and reduced material quality. Moreover, doping strategies to reduce the phase transition temperature typically increased thermal hysteresis and other adverse effects. As a result, the key challenges in VO_2 fabrication remain: the high transition temperature, poor environmental stability, stringent process requirements, and elevated production costs.

3.2. Chalcogenides (GST)

Chalcogenide systems doped with tellurium exhibit non-volatile structural transformations between disordered amorphous states and ordered crystalline arrangements, a property that supports their technological applications in PCMDs.[72–74]

These materials enable stable, non-volatile data storage with minimal energy requirements due to their permanent phase transition, contrasting with VO_2's transient phase change, necessitating continuous external stimuli to maintain its altered state. GST materials, typically composed of germanium (Ge), antimony (Sb), and tellurium (Te) in varying stoichiometric ratios

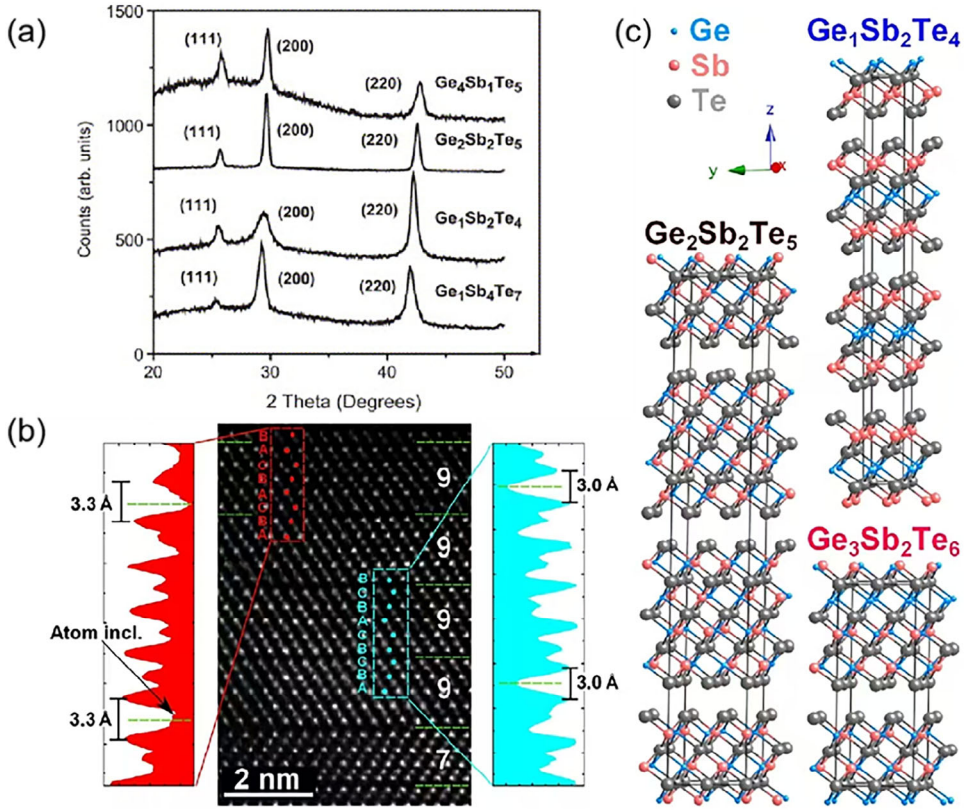

Figure 5. The structural analysis of GST. a) The XRD pattern of different composition GST alloys. Adapted with permission from.[78] Copyright 2005, Elsevier. b) High-resolution HAADF-STEM micrograph of GST alloys. c) Different schematic structures of GST alloys. Adapted with permission from.[77] Copyright 2016, Nature Publishing Group.

(commonly denoted as $Ge_2Sb_2Te_5$), belong to a class of PCMs characterized by reversible transitions between crystalline and amorphous phases triggered by heat, light, or electrical pulses. In the crystalline state, GST can adopt either a hexagonal structure (with lattice parameters a ≈ 4.23 Å and c ≈ 17.28 Å) or a face-centered cubic (fcc) arrangement, where Ge, Sb, and Te atoms form a layered, partially ordered lattice (as depicted in **Figure** 5c). Conversely, GST lacks long-range atomic order in the amorphous phase, featuring localized tetrahedral bonding configurations of Ge-Te and Sb-Te, as evidenced by extended X-ray absorption fine structure (EXAFS) studies.[75] Rapid heating through electrical pulses or laser irradiation induces the nucleation of metastable cubic crystallites (belonging to the space group *Fm-3m*), where Te atoms occupy 4a Wyckoff positions. In contrast, Ge/Sb atoms are statistically distributed across 4b sites, as confirmed by synchrotron X-ray diffraction.[76] This crystallization process follows a nucleation-dominated kinetics model, with activation energies ranging from 2.1 to 2.5 eV, derived from Arrhenius plots of time-dependent resistivity measurements. Notably, the cubic-to-hexagonal transition (space group $P\bar{3}m1$) typically occurs under prolonged thermal annealing. Figure 5a illustrates the XRD patterns of various GST alloy configurations, highlighting the corresponding peak positions. Additionally, Bragaglia et al.[77] utilized high-resolution HAADF-STEM (as shown in Figure 5b) to analyze the intergranular spacing and fundamental structural features of GST alloys. The phase transition in GST is rapid (occurring on the nanosecond scale) and highly reproducible, making it suitable for applications such as PCMDs and optical data storage (e.g., CDs and DVDs). The material's performance depends on the stability of the two phases, the speed of the transition, and the resistance contrast, all of which are influenced by its atomic structure and the thermodynamic conditions governing the phase-change process.

GST is celebrated for its capacity to execute rapid, durable, and reversible transitions between amorphous and crystalline states. This characteristic is utilized in various applications, including optical data storage and reconfigurable photonic systems. The phase transition induces substantial alterations in the material's physical attributes, positioning GST as a promising candidate for dynamic metasurfaces. During this transition, the atomic structure undergoes reorganization, shifting from a disordered amorphous state to an ordered crystalline configuration, typically occurring at temperatures ranging from 150 to 200 °C. This process can be thermally activated and is marked by changes in atomic bonding, essential for its distinctive properties. The phase change in GST is linked to latent heat and a notable variation in thermal conductivity. In its amorphous form, GST demonstrates lower thermal conductivity compared to its crystalline equivalent. This thermal behavior plays a critical role in applications that demand thermal management and energy efficiency, such as memory devices requiring swift heating and cooling cycles. In addition, upon heating beyond its melting point (≈600 °C) and

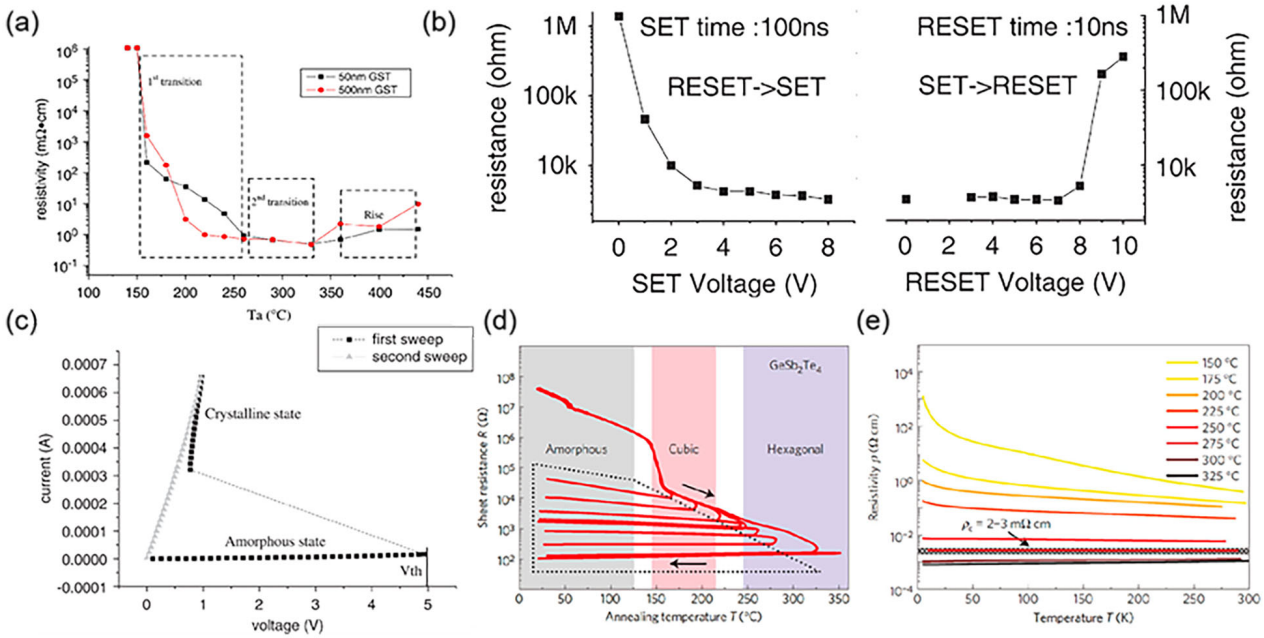

Figure 6. The relative properties of GST when the temperature changes. a) The Raman scattering pattern of GST alloys grown on silicon. b) The Resistance – Voltage characteristics of different phase change processes. c) GST voltage sweeping switching behavior. Adapted with permission from.[81] Copyright 2006, Elsevier. d) Temperature-dependent behavior of sheet resistivity in GST films with 100 nm thickness. Specimens underwent rapid thermal processing followed by 30-minute isothermal annealing at designated temperatures (150–325 °C) before natural cooling to ambient conditions. e) Electrical transport characterization of identical GST thin films under cryogenic conditions (5–300 K). Color differentiation in the panel indicates distinct thermal treatment histories, corresponding to eight crystallization states achieved through controlled annealing within the specified temperature window. Adapted with permission from ref. [72]. Copyright 2011, Nature Publishing Group.

undergoing ultra-rapid cooling, the crystalline structure of GST transforms into an amorphous form. Simultaneously, this transition significantly increases electrical resistivity, resulting in a notable decrease in optical reflectance. The distinct and fully reversible alterations in properties, combined with swift phase transition dynamics, make this material exceptionally appropriate for information storage systems and Blu-ray DVD technology.[79,80] In 2006, Lv et al.[81] illustrated the trend of resistivity fluctuations in GST thin films across various annealing temperatures. At 180 °C, the resistivity experienced a significant reduction for the first time, aligning with the crystallization of GST from an amorphous to a face-centered cubic (FCC) structure. As the temperature rises to 360 °C, resistivity decreases again, attributed to the phase transition from the FCC structure to a hexagonal arrangement (**Figure 6a**). They also investigated performance variations during the crystallization of GST via Joule heating (Figure 6b,c).[81] When the temperature surpasses 360 °C, there is an unusual rise in resistivity, potentially due to Ge oxidation or Te evaporation. GST thin films with a thickness of 500 nm exhibit a greater tendency toward crystallization compared to those with a thickness of 50 nm. This occurs because crystal nuclei in thicker films form and grow more stably under the dominant nucleation mechanism.

Moreover, one of the most pronounced modifications during the phase transition involves the optical properties of GST. Significant differences exist in refractive index and optical absorption coefficients between the amorphous and crystalline phases.[82] In its amorphous state, GST generally absorbs less light and possesses a lower refractive index. This tunability in optical characteristics is leveraged in metasurfaces for controlling light at varying wavelengths.[83] GST also demonstrates a significant difference in electrical conductivity between its amorphous and crystalline phases. The crystalline phase exhibits higher conductivity due to enhanced structural order and electron mobility, while the amorphous phase behaves more like an insulator. As shown in Figure 6d, when the temperature rapidly increases, GST alloys transition from an amorphous state to a cubic crystalline structure within the range of approximately 125–145 °C, accompanied by a dramatic change in resistance on the order of several magnitudes. As the temperature rises, the resistance decreases gradually until the crystal structure undergoes further changes. Siegrist et al.[72] observed that annealing at specific temperatures for 30 min, combined with low-temperature transport measurements (Figure 6e), reveals additional insights into this behavior. This characteristic is especially advantageous in electronic applications like PC memory, where data storage relies on the material's resistive states. The dynamic tunability of GST properties makes it highly suitable for use in tunable/reconfigurable metasurface devices.[84–87] Notably, Zalden et al.[88] utilized intense THz pulses to demonstrate that electron and lattice dynamics in GST occur on the picosecond timescale. These metasurfaces can manipulate electromagnetic waves in real-time, enabling applications such as adaptive lenses, beam steering devices, and tunable filters. Due to their intrinsic optical and electronic properties, phase-change chalcogenide alloys, particularly GST systems, exhibit remarkable compatibility with metasurface architectures.

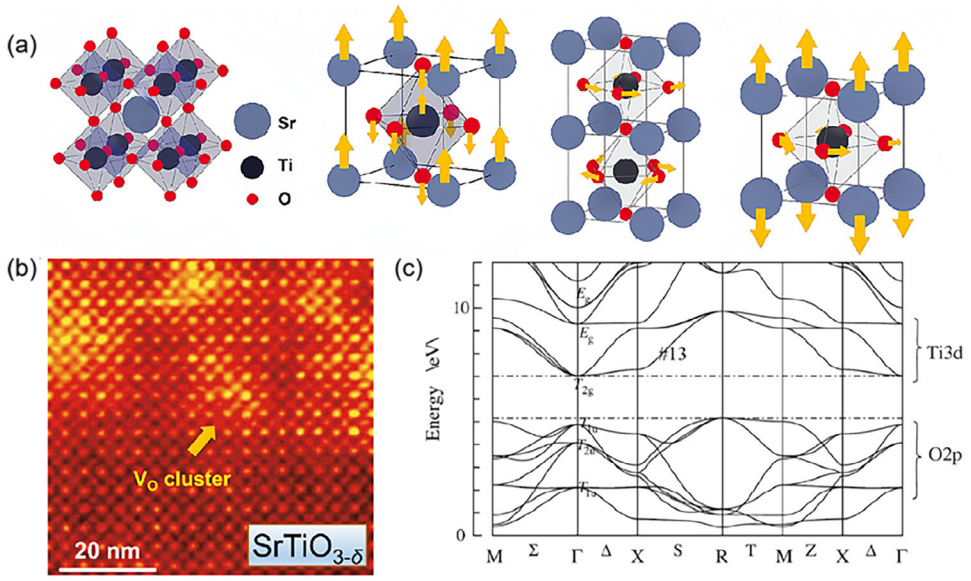

Figure 7. The crystal and band structures of STO PCMs. a) The schematic graph of ferroelectric displacement and AFD rotation in the STO structure, respectively. Adapted with permission from ref. [92]. Copyright 2009, Springer International Publishing AG. b) Atomic resolution high-angle annular dark-field (HAADF) scanning transmission electron microscopy (STEM) imaging reveals a structurally abrupt heterointerface between the stoichiometric $SrTiO_3$ substrate (lower region) and oxygen-deficient $SrTiO_{3-\delta}$ epitaxial layer (upper domain). Adapted with permission from.[93] Copyright 2004, Nature Publishing Group. c) The DFT calculation of the cubic phase STO. Adapted with permission from.[94] Copyright 2013, AIP Publishing.

Unlike VO_2-based systems, which require continuous external excitation, these chalcogenides offer non-volatile state retention and energy-efficient operation through reversible transitions between crystalline and amorphous phases. These non-equilibrium phase transition characteristics position these materials as ideal reconfigurable components for adaptive photonic metastructures and dynamically programmable optoelectronic interfaces. However, the fabrication and design of GST materials and devices demand high compositional accuracy and are susceptible to forming impurity alloys with electrode materials. Although GST materials exhibit advantages in terms of integration and endurance, enabling them to be more compatible with mass production using well-established sputtering techniques, their primary limitations compared to VO_2's ultrafast switching properties stem from lifespan restrictions caused by phase-change stress and elemental segregation.

3.3. Strontium Titanate ($SrTiO_3$, STO)

STO is a representative quantum paraelectric material, distinguished by a prominent anharmonic soft phonon mode that primarily governs its dielectric characteristics. The temperature-dependent behavior of this soft mode, which experiences a substantial frequency reduction upon cooling, plays a critical role in determining the material's low-frequency dielectric response.[89] At room temperature, STO exhibits an idealized cubic symmetry (space group *Pm-3m*), with strontium ions positioned at the corners of the unit cell, titanium ions at the body center, and oxygen ions at the face-centered locations. This crystalline arrangement demonstrates exceptional structural stability, although subtle distortions appear at lower temperatures, leading to a tetragonal phase transition. Specifically, STO maintains a cubic perovskite structure (space group $Pm\bar{3}m$) at room temperature. However, when cooled below approximately 105 K, it transitions to a tetragonal phase (space group *I4/mcm*). This transformation is driven by antiferrodistortive (AFD) rotations of oxygen octahedra and alternating rotations of adjacent octahedra around the cubic axes. These structural changes are linked to the softening of specific phonon modes, which substantially impact its dielectric properties.

STO is categorized as a quantum paraelectric material because it approaches ferroelectric instability but does not exhibit long-range ferroelectric order due to the suppression of quantum fluctuations.[90,91] These quantum effects stabilize the paraelectric phase even at cryogenic temperatures, where classical ferroelectricity typically emerges. As illustrated in **Figure 7a**, the schematic representation of STO's structure highlights the ferroelectric displacement and AFD rotation before and after the phase transition.[92] Mannhart et al.[93] utilized HAADF-STEM to reveal that STO under hypoxic conditions exhibits significantly altered structures (Figure 7b). According to density functional theory (DFT) calculations by Shirai et al.,[94] the valence band of STO is predominantly composed of oxygen 2*p* orbitals, with a bandwidth of ≈5–6 eV and its top located near the Γ point in Figure 7c. The conduction band, on the other hand, is primarily dominated by titanium 3*d* orbitals (mainly t_{2g} orbitals), with the bottom of the conduction band situated at the boundary of the Brillouin zone (such as *X* or *M* points), resulting in an indirect bandgap.

The dielectric behavior of STO is significantly shaped by its lattice dynamics, particularly the temperature-dependent characteristics of the anharmonic soft phonon mode.[95–97] As the temperature decreases, this mode experiences a gradual softening in frequency, which markedly enhances the low-frequency dielectric permittivity. This reflects the strong interaction between

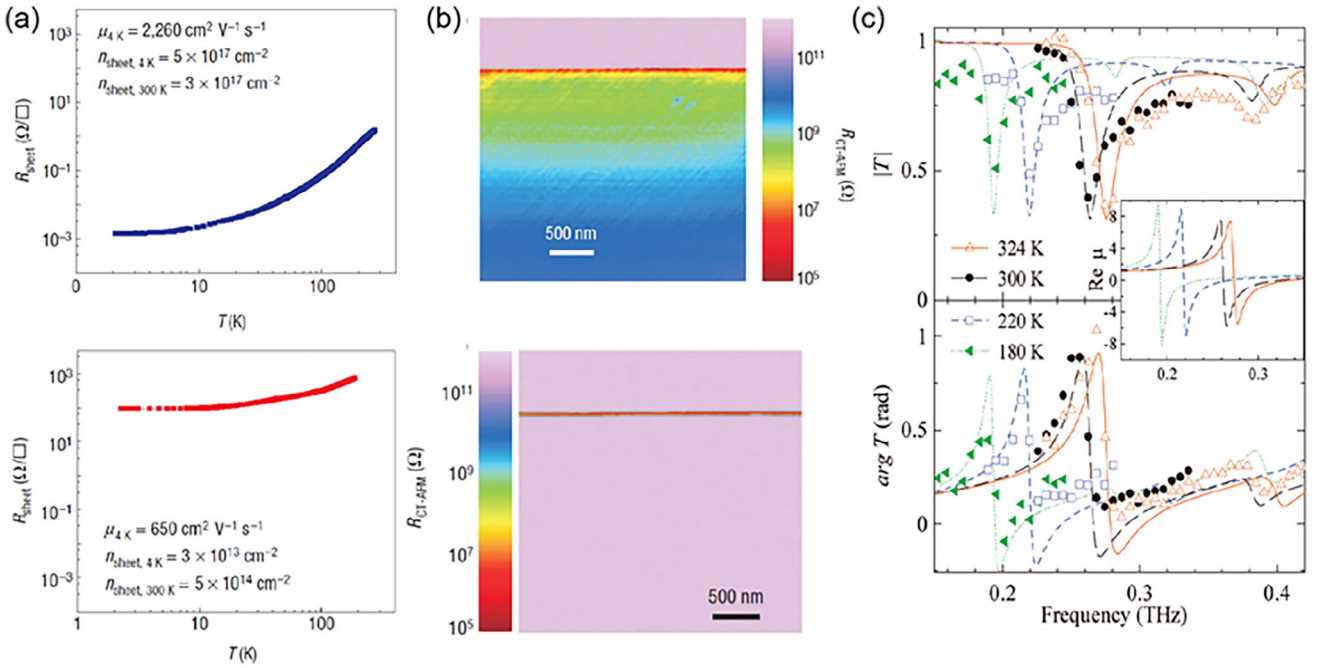

Figure 8. a) The resistance and carrier mobility under non-annealed and in-situ annealed conditions, respectively. b) CT-AFM resistance mapping. Adapted with permission from.[102] Copyright 2008, Nature Publishing Group. c) The transmission spectral response of the metamaterial, including both the magnitude and phase components, was examined at distinct temperature points. Adapted with permission from.[103] Copyright 2009, American Physical Society.

lattice vibrations and dielectric properties, highlighting the importance of anharmonicity within the phonon spectrum.[98–100] Additionally, the synergy between quantum fluctuations and anharmonic lattice dynamics inhibits the formation of ferroelectric order, preserving the quantum paraelectric state. These distinctive structural and dynamic features make STO an ideal model system for investigating the interplay of quantum effects, phonon softening, and dielectric responses in perovskite oxides. Recently, Asif et al.[101] employed a combination of the Lorentz model and the transfer matrix method to measure STO thin films' transmittance and refractive index.

In brief, STO's ferroelectric phase transition properties and mechanisms exemplify the complex interactions among quantum effects, lattice dynamics, and external perturbations. Although bulk STO does not exhibit long-range ferroelectric order under normal conditions, strain, doping, or low-dimensional engineering can modulate its polar behavior. As illustrated in **Figure 8**a,b, Basletic et al.[102] demonstrated the temperature-dependent sheet resistance of the non-annealed $LaAlO_3/SrTiO_3$ heterostructure at cryogenic temperatures (≈4 K). Interestingly, during the annealing process, conducting-tip atomic force microscopy (CT-AFM) resistance mapping revealed that the STO substrate exhibited overall insulation ($R > 10^{12}$ Ω), significantly higher than the resistance ($R \approx 5 \times 10^{10}$ Ω) in the unannealed state (where the STO substrate still maintained partial conductivity). Additionally, Němec et al.[103] reveals the transmittance spectra at varying temperatures and alongside theoretical simulations in Figure 8c. This indicates that the annealing process effectively suppressed oxygen vacancy diffusion, reducing the sample's conductivity. Nevertheless, since STO is inherently a quantum paraelectric at room temperature, achieving stable ferroelectricity requires defect engineering (e.g., oxygen vacancy manipulation) in conjunction with strain tuning. As a result, the computational modeling of high-temperature oxygen vacancy migration dynamics and equilibrium oxygen concentration becomes essential for guiding synthesis strategies. The primary goal in STO fabrication is to address its quantum paraelectric limitations. Major challenges involve the stringent demands for precise defect-strain synergistic engineering, insufficient thermal stability during operation, and high manufacturing costs.

3.4. Liquid Crystals (LCs)

LCs represent a unique state of matter that bridges the characteristics of conventional liquids and solid crystals. Structurally, they consist of anisotropic molecules, often rod-shaped or disc-shaped, allowing varying degrees of orientational and positional order. Unlike isotropic liquids, where molecular orientation is entirely random, LCs exhibit a degree of molecular organization that sets them apart as a distinct phase.[104–106] LCs are renowned for their diverse phase transition behaviors, typically triggered by temperature changes or external influences such as electric fields.[107–109] These transitions involve shifts in molecular ordering, as illustrated in **Figure 9**.[110] The hallmark of liquid crystals lies in their molecular arrangement and alignment. As the temperature decreases, molecules evolve from a disordered isotropic liquid into a nematic phase characterized by orientational order. This represents a first-order thermotropic phase transition, often accompanied by discontinuities in thermodynamic properties

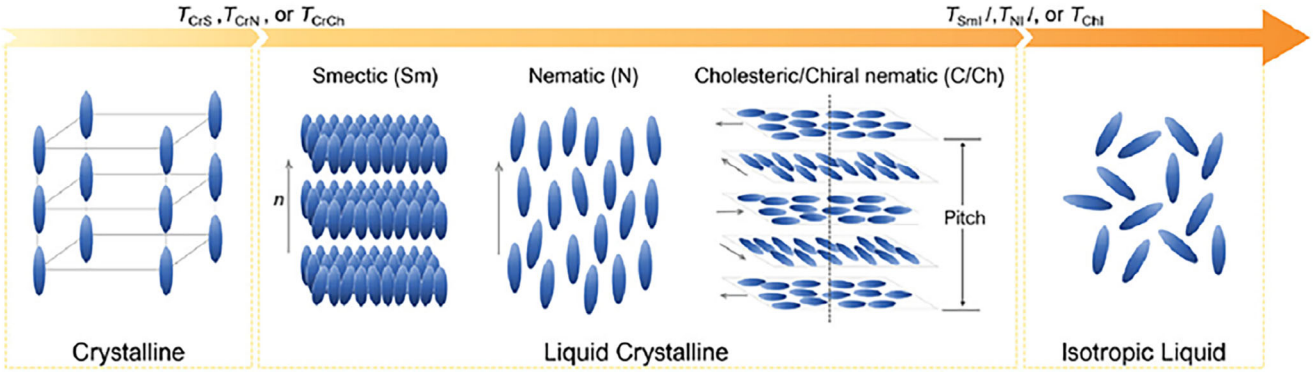

Figure 9. The typical mesogen alignment in smectic (Sm), nematic (N), and cholesteric (Ch) mesophases of LC. Adapted with permission from.[110] Copyright 2023, Wiley.

like enthalpy. Upon further cooling, the nematic phase may transform into the more ordered smectic phase, typically a second-order transition depending on the system and conditions. These phase transitions are governed by subtle variations in molecular interactions and exhibit critical phenomena, such as scaling of order parameters and pretransitional fluctuations. Moreover, liquid crystal phase transitions frequently involve changes in optical properties, including birefringence.[111] Their capacity to transition between different levels of molecular order under varying environmental conditions has positioned them as a fundamental component of modern material science. Ongoing research into their structural and thermodynamic properties continues to drive innovative applications in THz technology, ranging from modulators and displays to advanced sensing systems.[112–115]

LCs are extensively investigated for their anisotropic physical properties, which can be adjusted and controlled using external stimuli such as electric fields, magnetic fields, temperature variations, or light exposure. In temperature and light modulation, the observed sensitivity originates from the strong thermal reactivity of LCs molecular alignment. Temperature changes can easily trigger phase transitions, which substantially affect the level of molecular order and, consequently, modulate optical characteristics. For example, thermally responsive smart windows leverage these transitions to control light transmission by switching between a transparent state at cooler and a scattering state at higher temperatures.[116] Nevertheless, compared to voltage-driven modulation, this method demonstrates slower response dynamics and requires more energy. Additionally, the absorption of light energy can generate localized heating, offering an indirect mechanism to induce LC phase transitions. Although this non-contact modulation technique can achieve ultra-high resolution, its response speed is fundamentally constrained by thermal diffusion. This variety in control mechanisms underscores the significance of liquid crystals as a key material for intelligent optical devices, continuously broadening their application scope in THz technology. Among their diverse physical and electrical characteristics, their interaction with THz radiation has drawn considerable interest due to potential applications in THz technologies, including modulators, filters, and sensors. Importantly, LCs exhibit birefringence as a result of their anisotropic molecular structures. The refractive index varies depending on light's polarization and propagation direction relative to the molecular alignment, making this property crucial for controlling electromagnetic waves across various frequency ranges. Park et al.[117] visually showcased the differences in optical properties among various LC materials within the THz frequency band by analyzing frequency-domain data of refractive index and absorption coefficient (**Figure 10**a,b). This study highlights that material selection must balance birefringence, absorption, and response speed. This behavior may stem from the polarization response of LC molecules in the THz frequency range, where molecular polarization becomes more active at higher frequencies, leading to a slight increase in the refractive index. Recently, Fu et al.[113] utilized liquid crystals' dielectric tunability and birefringence effect to dynamically manipulate THz beams (Figure 10c). However, challenges persist regarding response speed and loss. As shown in Figure 10d, the response time of LCs is approximately 100 ms.[118] This is because, unlike the electronic or atomic restructuring observed in VO_2 or GST, LCs require molecular reorientation, which is influenced by factors such as viscosity, resulting in longer phase transition times. Undoubtedly, the dielectric dispersion and anisotropic properties of LCs enable them to regulate THz wave propagation by altering molecular arrangement through external fields. This phenomenon arises from the orientation-dependent response of molecular dipoles to electromagnetic waves.

As shown in **Table 1**, a comparative analysis of three representative PCMs highlights their unique operational features. While GST relies on a polycrystalline phase transition mechanism, VO_2 exhibits significantly faster switching speeds (on the sub-picosecond scale), making it an attractive option for THz ultrafast modulation applications. Nevertheless, its practical application is limited by thermodynamic challenges due to high critical temperatures, which necessitate additional energy inputs (such as thermal, electrical, or optical excitation) to trigger phase changes. Furthermore, while VO_2 exhibits a rapid phase transition, GST and LC provide non-volatility at the cost of higher driving voltages and longer phase-switching times. It should be noted that the selection of appropriate applications must be guided by the four specific parameter requirements outlined in the Table. For instance, the modulation frequency of a device in the THz range is determined by its dielectric constant and switching time. In contrast, the modulation depth is critically influenced by its conductivity. Meanwhile, the phase transition temperature

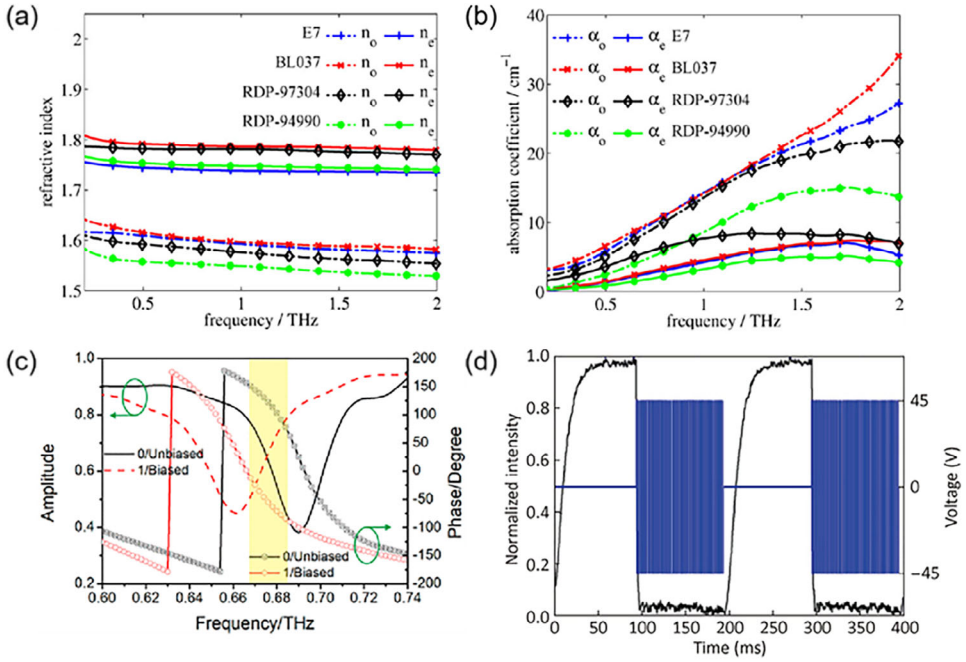

Figure 10. The corresponding properties of LCs. a,b) Refractive indices and absorption coefficients under 294 K. Adapted with permission from.[117] Copyright 2012, Optica Publishing Group. c) The amplitude and phase of LC under different dielectric constants. Adapted with permission from.[113] Copyright 2022, American Chemical Society. d) The response time of LCs under external 45 V. Adapted with permission from.[118] Copyright 2018, Optica Publishing Group.

determines the required operational power consumption. Therefore, selecting suitable materials for THz applications requires a comprehensive evaluation of these critical parameters. Additionally, VO_2's volatile switching behavior differs markedly from GST's non-volatile data retention capability and STO's field-driven operational mechanism. This three-way comparison emphasizes key research priorities: achieving an optimal balance among spectral operating ranges, electromagnetic transmittance, and dynamic conductivity modulation (>10^3 S m^{-1}), while addressing inherent material limitations through hybrid designs or interfacial engineering strategies.

4. Structure Design, Fabrication, and Performance Optimization

4.1. VO_2-Based PCMDs

As outlined in Section 3.1, the development of VO_2-based metasurfaces has attracted considerable interest due to the material's distinctive thermally driven IMPT, which enables dynamic modulation of optical properties on the picosecond timescale. Yang et al.[131] successfully demonstrated wide-angle symmetrical dual-beam scanning across a ±60° range using the

Table 1. The relative properties of various PCMs.

Materials	Dielectric Constant	Conductivity (S m^{-1})	Switching Time	Absorptivity/ Transmissivity	Switching Temperature	Refs.
VO_2	3.9	$2 \times 10^5 \rightarrow 10$	N/A	99.3%→15%	N/A	[119]
	3.5	2×10^5	Ultrafast	95%→30%	≈68 °C	[120]
	N/A	$2 \times 10^5 \rightarrow 10$	Ultrafast	98%	340 K	[121]
	3.85	$2 \times 10^5 \rightarrow 200$	N/A	N/A	68 °C	[122]
GST	N/A	948→300000	Fast	0.88→0.20	150/260 °C	[123]
	N/A	N/A	Fast	99%→30%	150/300 °C	[124]
	6.25/3.7	1500/4000	≈1ns	N/A	150/300 °C	[125]
STO	250/20000	Low	N/A	30→15	150→490 K	[126]
	185→252	N/A	Slow	N/A	N/A	[127]
	9.6	5.7×10^7	Slow	99.8%→2.1%	200 – 500 K	[128]
LC	2–10	10^{-11}	N/A	N/A	<50 °C	[129]
	≈18/6	≈1	Slow	N/A	30 °C	[130]

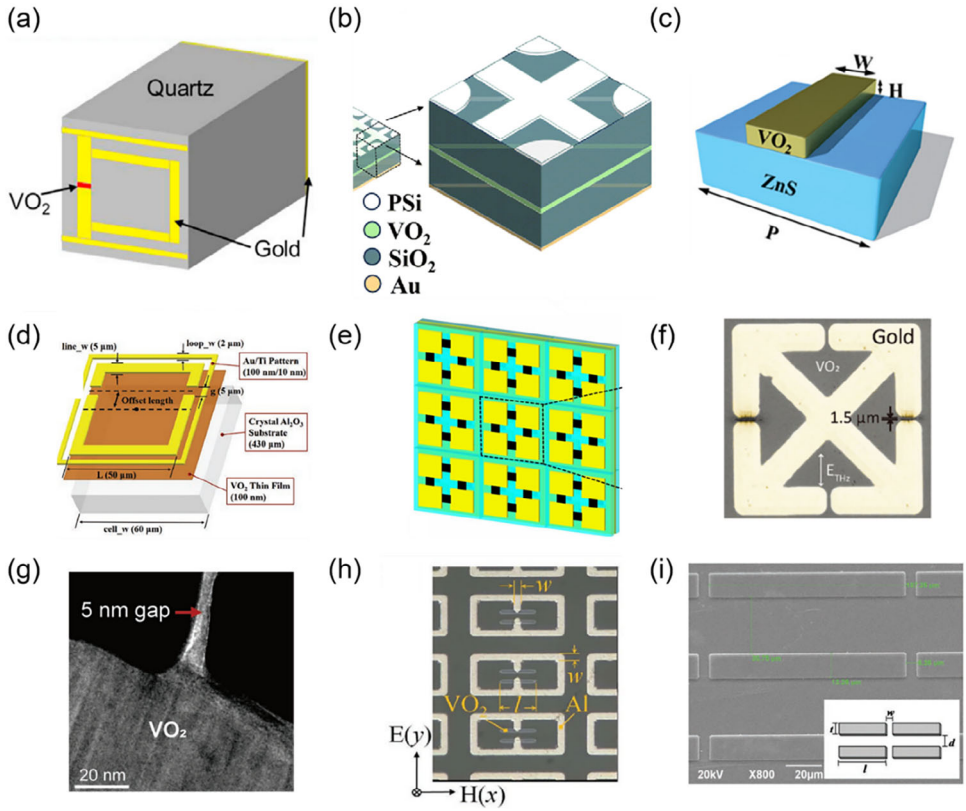

Figure 11. Preparation of different-shaped metasurfaces based on VO_2. a) The VO_2 metasurface modulates the deflection angles. Adapted with permission from.[131] Copyright 2022, Elsevier. b) Schematic image of multilayer metasurface. Adapted with permission from.[135] Copyright 2024, The Royal Society of Chemistry. c) Schematic diagram of polarization imaging metasurface. Adapted with permission from.[134] Copyright 2023, Wiley. d) Schematic of an asymmetric split-loop resonator with an outer square loop (ASLR-OSL) based on VO_2. Adapted with permission from.[137] Copyright 2018, Optical Society of America. e) Schematic picture of VO_2-based metasurface filter. The yellow and black units represent copper and VO_2, respectively. Adapted with permission from.[136] Copyright 2024, IOP Publishing. f) Optical image of metamaterial with a 1.5 μm gap deposited on VO_2/sapphire, elucidating the damage to the metasurface influenced by the vertically polarized THz field. Adapted with permission from.[139] Copyright 2012, Nature Publishing Group. g) TEM image of a 5 nm gap fabricated on a 100 nm thick VO_2 film. Adapted with permission from.[138] Copyright 2015, American Chemical Society. h) SEM image of a nanopattern. The periods along the x- and y-axes are 60 and 35 μm. Adapted with permission from.[140] Copyright 2015, Optical Society of America. i) SEM image of a VO_2 array with measured parameters of l = 107.25, w = 6.25, d = 30.75, and t = 13.25 (all units in μm). Adapted with permission from.[141] Copyright 2010, AIP Publishing.

configuration illustrated in **Figure** 11a and achieved femtosecond-scale response times through external electrical stimulation. Creating such functional platforms involves various fabrication techniques, broadly classified into thin-film deposition methods, lithographic patterning approaches, and post-processing treatments. Below is a systematic exploration of these strategies, focusing on their adaptability for achieving tailored optical responses in VO_2 metasurfaces. Fabrication requires precise control over the VO_2 phase transition behavior and nanoscale patterning.

Physical vapor deposition (PVD) is a dominant technique in this field, with magnetron sputtering a prominent example. This method enables the preparation of large-area uniform thin films and offers versatile doping capabilities, such as incorporating tungsten (W) or molybdenum (Mo) to adjust phase transition temperatures.[132] However, it often demands high-temperature annealing. Despite this limitation, PVD is widely adopted due to its scalability and ability to produce films with superior uniformity and adhesion. Lately, Ivanov et al.[133] synthesized epitaxial W-doped VO_2 films via a solvothermal method followed by post-annealing treatment. This approach yielded a notably depressed phase transition temperature approaching room temperature (≈31 °C) while maintaining a substantial THz modulation depth of approximately 60.5%. For instance, Li et al.[66] used magnetron sputtering to prepare a 20 nm homogeneous VO_2 thin film on mica, which exhibited exceptional detection response. Nevertheless, the need for high vacuum and potential deviations in oxygen content may result in the formation of undesired VO_2 phases. Alternatively, Ma et al.[134] utilized PLD technology to deposit 250 nm thick VO_2 thin films using a 248 nm KrF excimer laser under 0.25 Pa oxygen atmosphere and room temperature conditions, yielding a linear polarization extinction ratio (LPER) of 10 dB. These metamaterial advances establish a framework for miniaturized thermal polarization imaging systems (Figure 11c). A metasurface layer was introduced to control the dip-coating rate and annealing conditions. This sol–gel method involves the hydrolysis and polymerization of metal alkoxides or metal chlorides to form a colloidal suspension, which is subsequently deposited

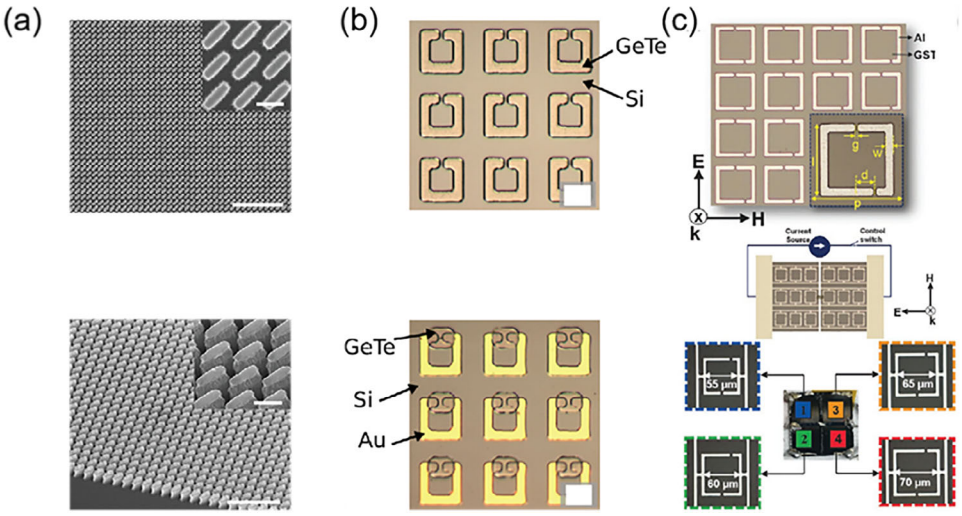

Figure 12. Different design methodologies of metasurfaces based on chalcogenide PCMs. a) SEM images of the fabricated reconfigurable THz metasurfaces. The inner scale bar is 500 nm. Adapted with permission from ref. [146]. Copyright 2024, Wiley. b) gold with additional GeTe films. Adapted with permission from ref. [147]. Copyright 2016, AIP Publishing. c) Fabricated GST Fano metadevice (GFMD). The parameters of the schematic graph are p = 75 μm, l = 60 μm, w = 6 μm, g = 3 μm, and d = 15 μm. Schematics of electrically switched GFMD with entire unit cells electrically attached to bond pads. Adapted with permission from ref. [148]. Copyright 2019, Wiley.

onto a substrate. The sol–gel process is advantageous due to its low cost and ability to produce uniform coatings over large areas. However, ensuring precise stoichiometry and crystallinity of VO_2 remains challenging. Generally, due to the attenuation of THz in air, the modulation range is limited, but Fu et al.[135] used metamaterials structure in Figure 11b realized the high absorptivity rate in the dual-broadband of 2.47–3.71 THz and 8.90–10.62 THz. Additionally, Wang et al.[136] and Park et al.[137] both utilized the high conductivity nanoantennas in Figure 11d,e, which achieved the highly efficient THz transmission under external stimuli. Nevertheless, the gap width in metamaterials will greatly limit the performance of the device (1.5 μm in Figure 11f and 5 nm in Figure 11g), as the THz signal is too concentrated in this area, leading to material damage.[138,139] Moreover, by incorporating parallel-plate capacitors within the gaps of split-ring resonator (SRR) structures, Meng et al.[140] demonstrated effective compensation for resonant frequency shifts caused by various near-field coupling effects (Figure 11h). It is worth noting that the implementation of cut-wire resonators significantly enhanced THz absorption at the resonant frequency in early-stage designs that lacked additional metallic antenna structures, as shown in Figure 11i.[141]

Other synthesis methods, such as molecular beam epitaxy (MBE) and pulsed laser deposition (PLD), are commonly used for thin-film preparation. MBE achieves atomic-level thickness control but is constrained by slow growth rates and high costs, making it more suitable for theoretical studies or integration with 2D materials. It provides atomic-scale control over film thickness and composition.[142,143] Emerging hybrid techniques, such as self-assembly templating or femtosecond laser direct writing, enable sub-50 nm patterning or reconfigurable metasurfaces without masks. Key challenges include reducing processing temperatures (<300 °C) for compatibility with complementary metal-oxide-semiconductor (CMOS) technology, enhancing dynamic modulation (e.g., THz modulation depth > 90%), and scaling up production via methods like nanoimprint lithography.[144,145]

Advancements in these areas could lead to breakthroughs in 6G communications, adaptive infrared camouflage, and energy-efficient smart windows, positioning VO_2 metasurfaces at the forefront of next-generation optoelectronic technologies. As shown in Figure 11, various patterns and nanoantennas under different designs are utilized for wavefront modulation in the THz regions.

4.2. GST-Based PCMDs

A widely adopted method for fabricating GST nanostructures involves combining lithography with electron beam deposition or sputtering techniques. This approach enables precise control over the geometry and thickness of GST layers, allowing for customized optical properties tailored for photonic routing applications. For instance, Li et al.[83] deposited a 550 nm α-Si film using inductively coupled plasma-enhanced chemical vapor deposition (PECVD) at 130 °C and sputtered a 250 nm GST layer at room temperature (**Figure 12a**).[146] They successfully fabricated GST/α-Si bilayer metasurfaces by integrating electron beam lithography with ICP-RIE etching, magnetron sputtering, and PECVD thin-film deposition technologies. This process achieved efficient modulation of cross-polarized light. However, this method can be resource-intensive due to the high-resolution demands for intricate metasurface designs. Additionally, as shown in Figure 12b, Kodama et al.[147] entirely composed of 300 nm-thick GeTe films deposited via RF magnetron sputtering onto intrinsic silicon substrates and utilized a bilayer photolithography process. To date, high-performance electrically driven reprogrammable GST metasurfaces have been developed through RF magnetron sputtering to deposit a 200 nm thick GST layer, as shown in Figure 12c.[148] Notably, an atomic layer

deposition (ALD) process was employed to grow a 100 nm thick hafnium oxide (HfO_2) layer on the surface as a thermal isolation layer. A 100 nm thick gold electrode was then deposited via electron beam evaporation (E-beam) to establish electrical contact with a microheater. This technique ensures excellent symmetry and uniformity of the structures, making it suitable for applications requiring high reproducibility. Nevertheless, its limited design flexibility may not accommodate the arbitrary geometries necessary for advanced photonic routing. Furthermore, achieving optimal performance in GST alloys remains challenging due to the strict requirements for precise composition and control of the stoichiometric ratio. During etching processes, the high selectivity of GST often leads to undesirable chemical residue.[149,150] Additionally, thermal evaporation deposition frequently fails to provide adequate conformal coverage on device sidewalls.[150] The deposition of dielectric encapsulation layers via ALD—used to reduce substrate thermal losses and improve heat transfer—typically requires process temperatures below 200 °C.[151] This limitation arises because elevated thermal processing can induce unintended crystallization in GST, thereby complicating the realization of uniform thermal distribution across larger areas.

In summary, selecting a preparation method depends on the specific application requirements, such as desired resolution, scalability, material compatibility, and structural complexity. Lithography-based techniques are renowned for their precision in microfabrication but often involve significant resource allocation. In contrast, nanoimprint lithography offers a cost-effective alternative that balances economic feasibility with large-scale manufacturability. Meanwhile, self-assembly approaches excel in generating periodic nanostructures with inherent uniformity, though their applicability is restricted when addressing complex, aperiodic architectural needs. Each methodology presents unique advantages and limitations that must be carefully assessed against the specific parameters of nanoscale fabrication tasks.

4.3. STO-Based PCMDs

The creation of STO MDs employs various techniques, each designed to achieve specific structural and material properties essential for advanced optical and dielectric functionalities. One commonly used method is solution-based spin coating, which is particularly well-suited for developing flexible metasurfaces. This process typically involves preparing a composite solution where STO nanopowders are uniformly dispersed within a polymeric matrix, such as polyimide, to form a hybrid material. The solution is then deposited onto a substrate using spin coating to ensure the formation of a uniform thin film. Subsequent steps include photolithography for defining metallic patterns and removing sacrificial layers to isolate the desired structures. Protective coatings may also be applied to enhance the mechanical durability of the fabricated metasurface. This method is advantageous due to its cost-effectiveness and simplicity, making it ideal for integrating STO's high dielectric properties with flexible substrates. Recently, Wang et al.[152] developed two THz flexible metasurfaces based on an STO/polyimide (PI) substrate, demonstrating stable amplitude tunability with temperature changes ranging from 290 to 590 K.

In contrast, sputtering techniques are often employed for depositing STO thin films, especially when high crystalline quality is required for integration with other functional materials. This process involves physical vapor deposition of STO in a controlled atmosphere, typically a mixture of argon and oxygen gases, to regulate film stoichiometry and crystallinity. Before deposition, substrate preparation is crucial to ensure surface smoothness and compatibility. Using buffer layers, such as titanium dioxide (TiO_2) or magnesium oxide (MgO), is essential for reducing lattice mismatch and minimizing interdiffusion at the interface, thereby optimizing the crystallographic alignment and electronic characteristics of the STO layer. The unique STO metamaterials can conduct the thermal tunability in the THz realm (**Figure 13a**), achieving dual dynamic control of terahertz wave amplitude and frequency and synchronous amplitude control with a maximum modulation depth of 29.8%.[153] Meanwhile, the metadevice based on STO (Figure 13b) can also realize magnetic response and tuning by temperature controlling the dielectric constant of STO in 0.2 – 0.36 THz. Interestingly, Bian et al.[127] and Wu et al.[154] all utilized the square open structure of PCMDs in Figure 13c,d, respectively. Together, they underscore the versatility of ferroelectric-based MDs in bridging material properties and electromagnetic functionality. Achieving high-quality STO films requires careful optimization of growth parameters, including deposition temperature, gas pressure, and sputtering power. When adapted for STO, these techniques offer new possibilities for designing metasurfaces with complex geometries and tunable optical responses. Additionally, polarization-sensitive metasurface designs often leverage continuous phase control and precise material anisotropies, highlighting the versatility of STO for advanced photonic applications.

In summary, the fabrication of STO MDs encompasses a range of methodologies, each with unique advantages and limitations. Solution-based techniques like spin coating are expensive and flexible, while sputtering provides superior crystalline quality for integrated systems. Together, these approaches emphasize the versatility of STO as a functional material, with each fabrication strategy tailored to meet specific structural, optical, and electronic requirements.

4.4. LCs-Based PCMDs

Metamaterials and MDs based on LCs have become revolutionary platforms for THz modulation, driven by their unique phase transition properties and anisotropic molecular reorientation capabilities. Unlike traditional materials, which typically depend on rigid structural designs or transient carrier dynamics, LCs offer reconfigurable optical responses triggered by external stimuli such as electric fields, temperature changes, or light exposure. This adaptability arises from their inherent capacity to undergo phase transitions, like the nematic to isotropic phase shift, which induces substantial variations in refractive index and optical birefringence. These transitions allow for precise, real-time control of THz wave propagation and operate at relatively low power levels compared to alternative PCMs such as VO_2 or GST. Furthermore, the soft matter characteristics of LCs enable them to be

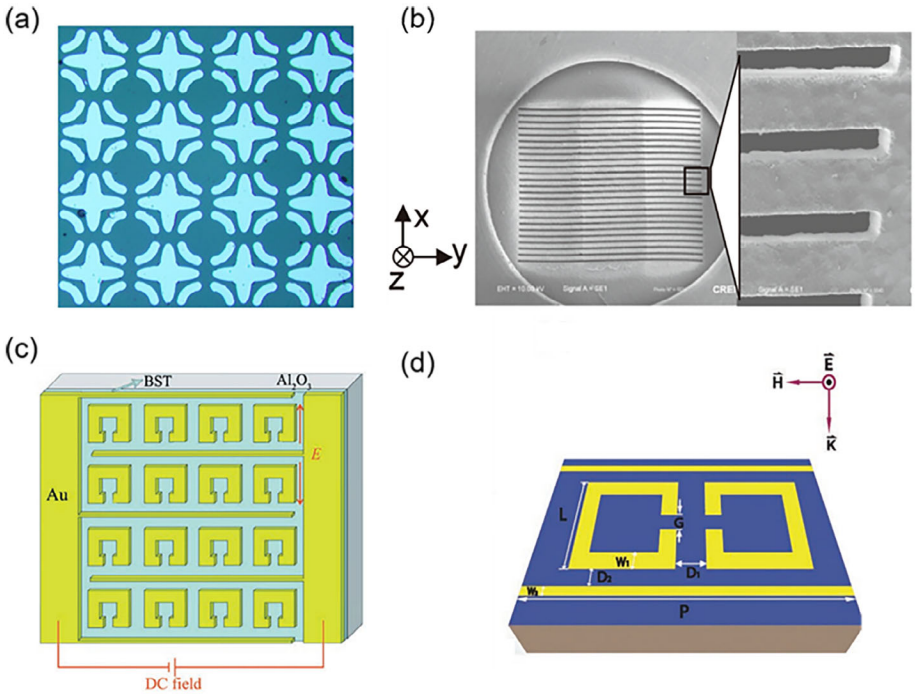

Figure 13. Microscopy and Schematic diagrams of different patterns based on ferroelectric material's metasurfaces. a) Optical image of the 300 μm STO metasurface array on SiO_2. Adapted with permission from ref. [153]. Copyright 2025, IOP Publishing. b) SEM image of a sample consisting of a row of high permittivity rods based on a STO thin single crystal plate. Adapted with permission from ref. [103]. Copyright 2009, American Physical Society. c) Interdigital electrode patterns were prepared on a thin barium strontium titanate (BST) film. Adapted with permission from ref. [127]. Copyright 2014, AIP Publishing. d) Schematic image of metasurface with a 5 μm gap. Adapted with permission from ref. [154]. Copyright Wiley.

seamlessly incorporated into flexible and tunable MDs, enhancing efficient modulation across a wide frequency spectrum. The scalability and reduced manufacturing complexity of LC-based systems further highlight their potential as a leading solution for next-generation THz technologies, especially in applications involving dynamic beam steering, adaptive filtering, and ultrafast signal processing.[155–157] In this context, Hao et al.[158] and Fu et al.[113] introduced self-powered THz modulation systems that integrate MDs. The design of these metamaterials and their interaction with LCs form the foundation of the THz wave modulation mechanism, enabling dynamic spectral reconfigurability (**Figure 14**a,b). Additionally, Wang et al.[159] demonstrated a resonant frequency shift from 0.75 to 1 THz and amplitude modulation of approximately 80% using graphene-integrated LC metadevice under a low driving voltage of 10 V (Figure 14c). Notably, as shown in Figure 14d, each pixel controlled by an electric field adjusts the orientation of LCs to tune absorption, achieving 75% reflectivity modulation and programmable spatial patterns at around 3.67 THz.[115] In Figure 14e, the fishnet metadevice addresses the issue of switching speed in LC-based systems.[160]

5. THz Regulations and Applications Based on PCMDs

5.1. Dynamic Modulation and Absorption Control

The reconfigurable metasurface demonstrates dynamically adjustable optical responses driven by phase transition mechanisms, such as thermally or electrically induced IMPTs, enabling real-time control of electromagnetic absorption characteristics in THz regimes.[161–166] This mechanism allows for a significant tuning range of absorption properties through crystallographic transformations. Wavefront modulation involves the dynamic manipulation of wave attributes, including amplitude, phase, polarization, or frequency, with applications spanning high-speed communication,[167] smart window,[168,169] and thermal regulation.[170,171]

In **Figure 15**a, Malevich et al.[172] introduced a scalable method for dynamic THz and millimeter-wave manipulation by integrating graphene-based electro-optical modulators with thin-film transistor arrays. They developed a reconfigurable intelligent surface consisting of over 300000 individually addressable subwavelength pixels (with a pitch of 185 μm), enabling programmable control of THz transmission and reflection. By utilizing bilayer graphene and electrolyte gating, the device achieved rapid modulation (with a switching time of 1 ms) and phase tuning via topological phase transitions near reflection singularities. The authors demonstrated its potential in single-pixel compressive imaging of concealed metallic objects and dynamic beam steering with orbital angular momentum generation, addressing key challenges in scalable THz technologies for next-generation communication and imaging systems.

Similarly, both Wang et al.[173] and He et al.[174] exploited the dynamic tunability of VO_2's conductivity through thermal excitation, enabling versatile control over THz waves. While their structural designs and targeted applications differ, these studies highlight the adaptability of VO_2 in THz device engineering. Figure 15b shows the transmittance spectra of the

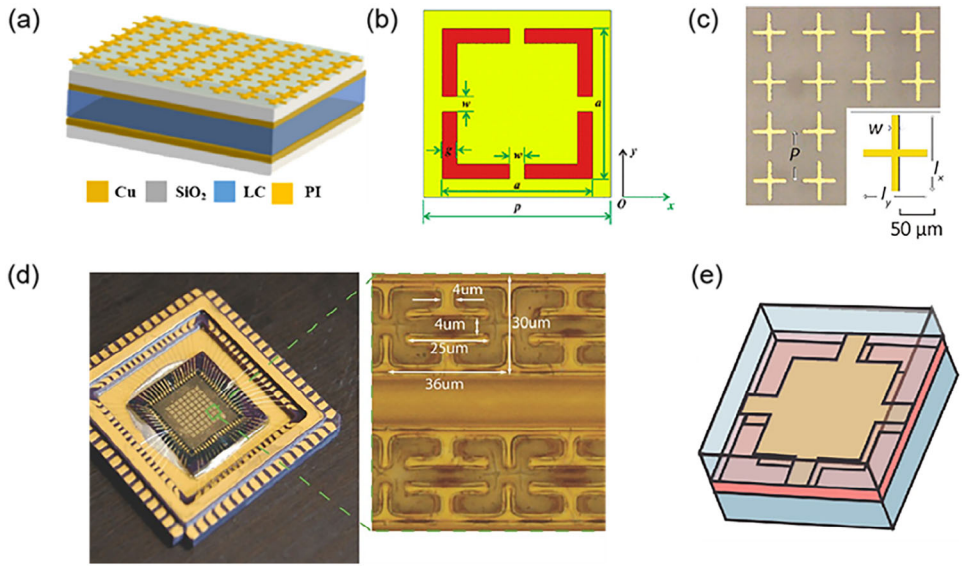

Figure 14. Microscopy and Schematic diagrams of different patterns based on LC metasurfaces. a) Schematic picture of the integrated LC cell and metasurfaces. Adapted with permission from ref. [158]. Copyright 2024, American Chemical Society. b) Schematic diagram of a metamaterial single cell of LC (p = 200 μm, a = 160 μm, and w = g = 16 μm).Adapted with permission from ref. [113]. Copyright 2022, American Chemical Society. c) Optical image of LC based reconfigurable metamaterial (P = 150 μm, lx = 120 μm, ly = 100 μm and w = 10 μm). Adapted with permission from ref. [159] Copyright 2017, Optica Publishing Group. d) Camera image of the THz modulator coated with LC. Adapted with permission from.[115] Copyright 2014, Wiley. e) Schematic picture of tunable THz metamaterial. Adapted with permission from ref. [160]. Copyright 2015, Nature Publishing Group.

proposed VO_2-based metadevice filter under varying conductivity states of VO_2, validated numerically using finite element method simulations.[173] When VO_2 is in its insulating state ($\sigma = 2 \times 10^2$ S m^{-1}), the filter exhibits an ultra-broadband bandpass response with a transmission coefficient exceeding 90% across the 1.07–3.78 THz range, achieving a relative bandwidth of 112%. The structure optimally controls the reflection phase gradient for linearly polarized (LP) and circularly polarized (CP) waves at low (1.34 THz) and high (2.53 THz) frequencies, respectively (Figure 15c).[174] It achieves cross-polarization conversion efficiencies of 98.86% for LP waves and 81.86% for CP waves.

Recently, Wu et al.[175] designed a tunable metasurface where the proposed VO_2 structure demonstrates broadband absorption characteristics with efficiency exceeding 90% across the 0.6–1.0 THz spectrum. This performance remains polarization-independent for both linear and circular electromagnetic wave excitations. The integration of phase-transition mechanisms with metasurface design principles in this platform enables dynamically reconfigurable optical responses, providing a modulation or absorbance depth greater than 80% and establishing a scalable framework for adaptive photonic systems across the mid-infrared (MIR), near-infrared (NIR), and THz spectral regimes.

5.2. Image Processing and Multitemporal Programming

Incorporating VO_2 into tunable and reconfigurable metasurfaces has introduced a revolutionary approach for dynamic wavefront manipulation across THz spectral regimes. This leverages its abrupt IMPT to enable multifunctional optical computing and adaptive sensing. Image processing involves analyzing, enhancing, and manipulating digital images to extract meaningful information, improve visual quality, or facilitate computational tasks such as object recognition, feature detection, and scene reconstruction. As imaging environments grow more complex, such as under dynamic lighting conditions, high-speed motion, or multispectral requirements, traditional imaging systems often struggle to adapt in real time, leading to suboptimal performance in critical applications.[176–179] Moreover, the increasing demand for real-time adaptability, energy efficiency, and miniaturization in programmable tasks has surpassed the capabilities of conventional materials and devices, driving the exploration of innovative materials and reconfigurable MDs.

In image processing, VO_2 can create tunable optical filters or smart sensors that dynamically adjust to varying environmental conditions. Additionally, due to its temperature-sensitive phase transition, VO_2 can trigger time-dependent or environment-responsive computational tasks when integrated into multitemporal programming frameworks. For instance, as shown in **Figure 16a**, conventional PIN diode-based reconfigurable approaches face significant limitations in achieving high-speed modulation within the THz regime. To overcome this challenge, an 8×8 VO_2 supercell array was employed, enabling single-beam anomalous reflection with directional control through phase gradient encoding. By applying the superposition theorem, the platform supports the generation of both symmetric and asymmetric multi-beam patterns, thereby integrating electrically triggered phase-transition mechanisms with digital coding methodologies. Moreover, switchable orbital angular momentum (OAM) mode vortex beams were generated using spiral phase encoding, while convolution operations were applied to achieve arbitrarily steerable multi-vortex beams.[180] In parallel, Zhang et al.[181] utilized non-PCMs to achieve ultrafast programmability in the THz region. A key application lies in high-speed optical computing

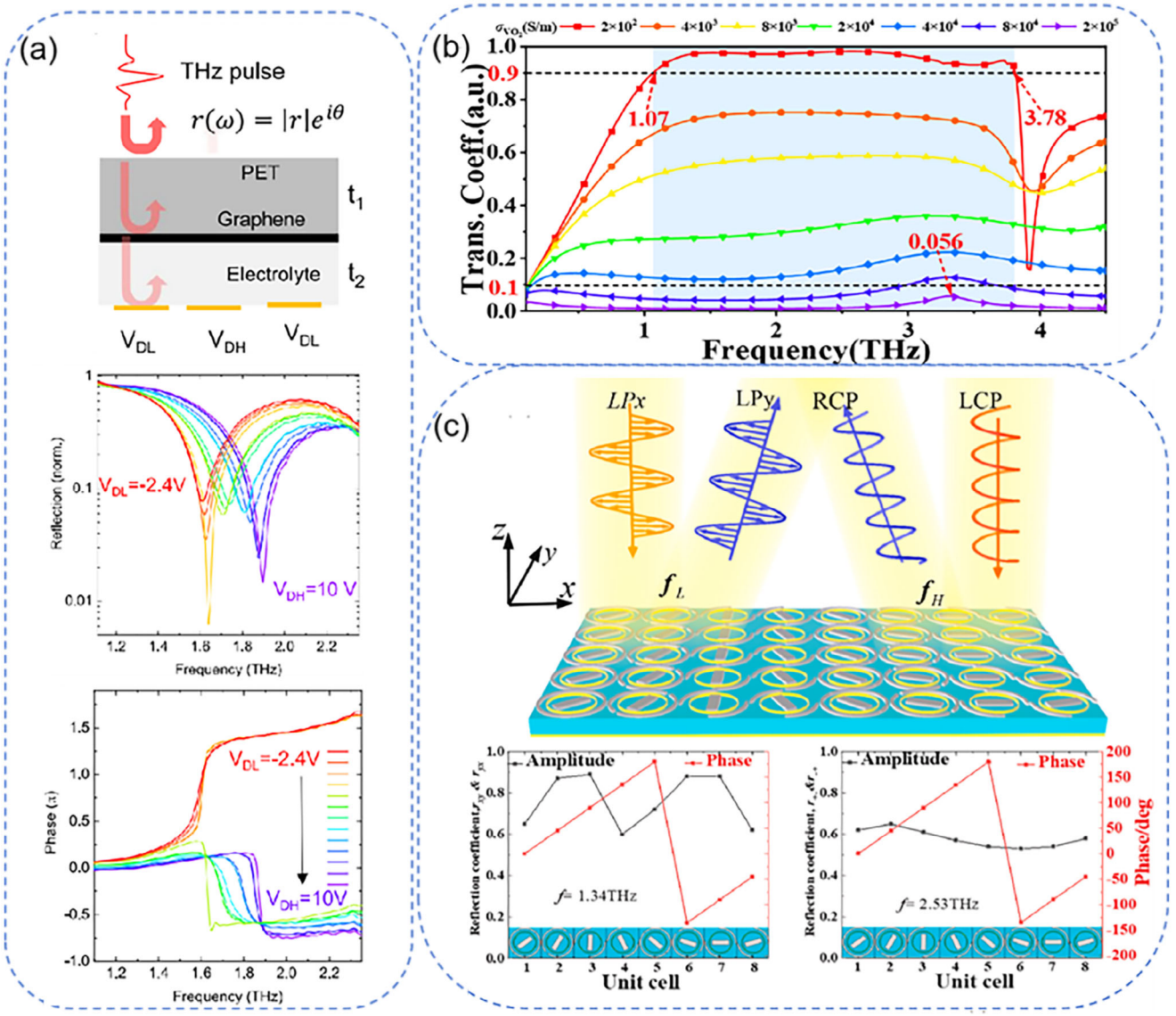

Figure 15. The dynamic modulation results from reconfigurable metasurfaces. a) The ability to achieve topological phase transitions near reflection singularities, enabling abrupt 2Π phase jumps. Adapted with permission from ref. [172] Copyright 2025, Nature Publishing Group. b) Transmittance spectra of VO_2 under varying conductivity states. Adapted with permission from ref. [173]. Copyright 2024, Elsevier. c) The structure and performance validation results of a tunable dual-polarization reflected THz beam deflector are presented. Adapted with permission from ref. [174]. Copyright 2024, Elsevier.

systems, where demonstrated logic gates (XNOR, NOR, OR) operating across switchable frequencies (0.73–1.24 THz) and time domains (1.25–4.75 ps transitions) could underpin architectures for asynchronous, parallel data processing. These capabilities are essential for addressing the growing demands of artificial intelligence and real-time analytics, where low latency and energy efficiency are paramount (Figure 16b). The ability of these MDs to independently manipulate spectral, temporal, and polarization degrees of freedom further supports multidimensional signal multiplexing—a fundamental requirement for next-generation 6G communications reliant on ultra-wideband THz channels.

On the other hand, metadevices based on PCMs integrate the advantages of both approaches, overcoming inherent limitations associated with traditional image and data processing, such as bottlenecks in processing speed, high energy consumption, and reliance on complex algorithms.[182–185] Notably, the photothermoelectric (PTE) effect provides hardware support for the intelligent processing of near-field sensors.[66] Under conditions where noise intensity exceeds 80% of the target signal, the detector achieves selective amplification of high-intensity signals and noise suppression by modulating the bias voltage. This approach enables dynamic intensity discrimination and nocturnal pattern recognition, as exemplified by the successful extraction of the high-intensity "U" pattern from superimposed "C" and "U" inputs in Figure 16c. Furthermore, Cotrufo et al.[186] combined PCM dynamics with nonlocal photonic design, bridging the gap

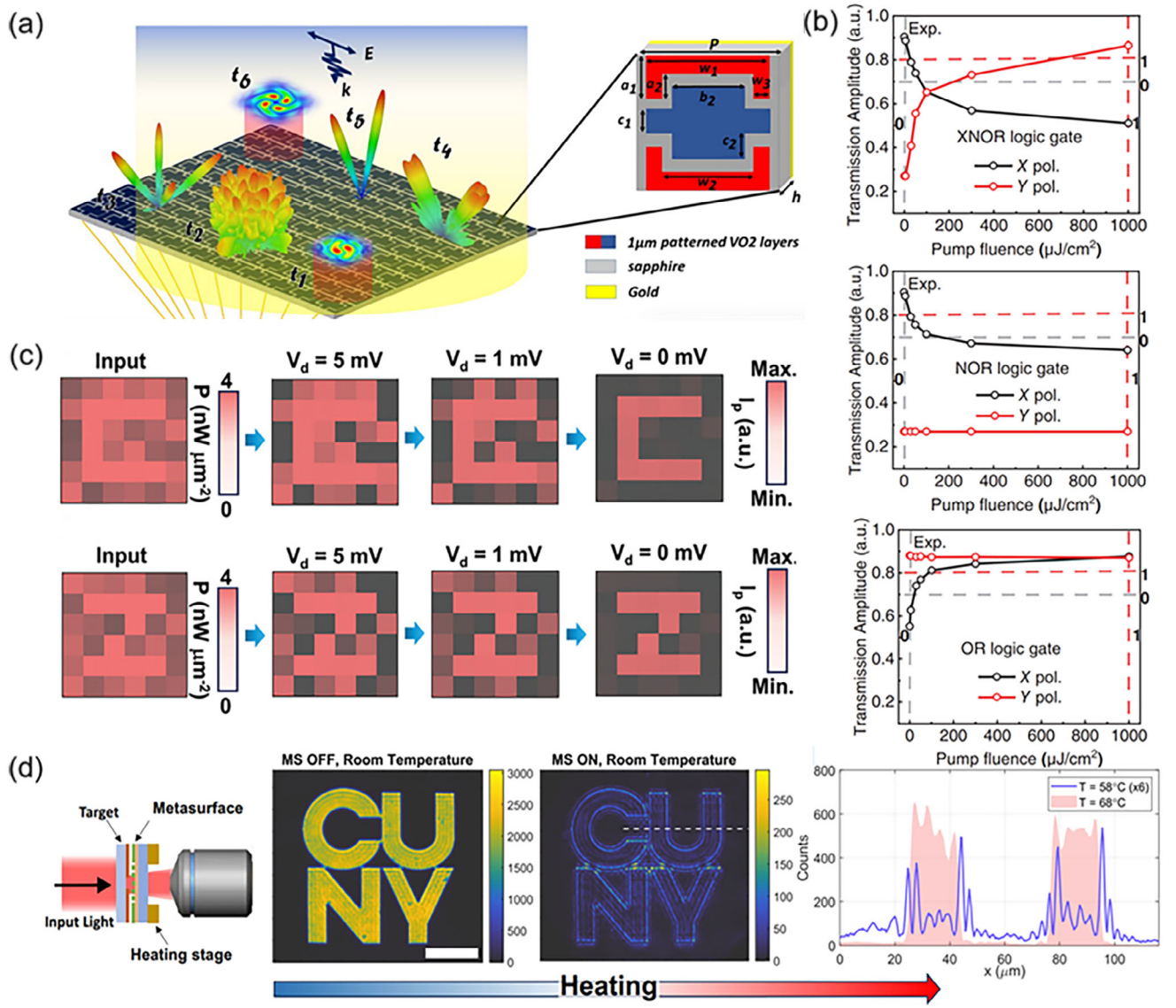

Figure 16. The frontend applications are based on reconfigurable metasurfaces. a) Schematic diagram of VO_2-based programmable coding metasurface. Loading spatial encoding sequences at different times. Adapted with permission from ref. [180]. Copyright 2020, Nature Publishing Group. b) The experimental results of three different logic gates under different THz frequencies. Adapted with permission from ref. [187] Copyright 2025, Wiley. c) The near sensor image processing capability of the VO2-based PTE detector under high noise input. Adapted with permission from ref. [66]. Copyright 2024, Wiley. d) Experimental schematic diagram and image input without metasurface. Adapted with permission from ref. [186]. Copyright 2025, Nature Publishing Group.

between static analog devices and adaptable computing systems. This offers a pathway toward ultra-compact, energy-efficient solutions for real-time optical computation. Experimental validation confirms the device's performance metrics. At 1665 nm, the metadevice achieves a numerical aperture of 0.26, enabling high-resolution edge detection with a spatial resolution of ≈3.2 μm. Throughput efficiencies of ≈10% were measured, comparable to state-of-the-art static MDs despite the added complexity of reconfigurability. Imaging experiments using amplitude masks (e.g., institutional logos and geometric shapes) demonstrated robust edge enhancement at low temperatures, with contrast ratios exceeding 10:1 (Figure 16d). However, considering the volatility of VO_2-based systems, GST-based image-processing MDs can solidify commonly used registration parameters, such as affine transformation matrices and feature point templates. This means the retentive properties of GST alloys can reduce redundant calculations, offering an advantage in computational efficiency.

5.3. Optoelectronic Metadevices and Biology Detection

Reconfigurable MDs in the THz regime have emerged as a groundbreaking technology within optics and biosensing, offering unparalleled control over light-matter interactions at the

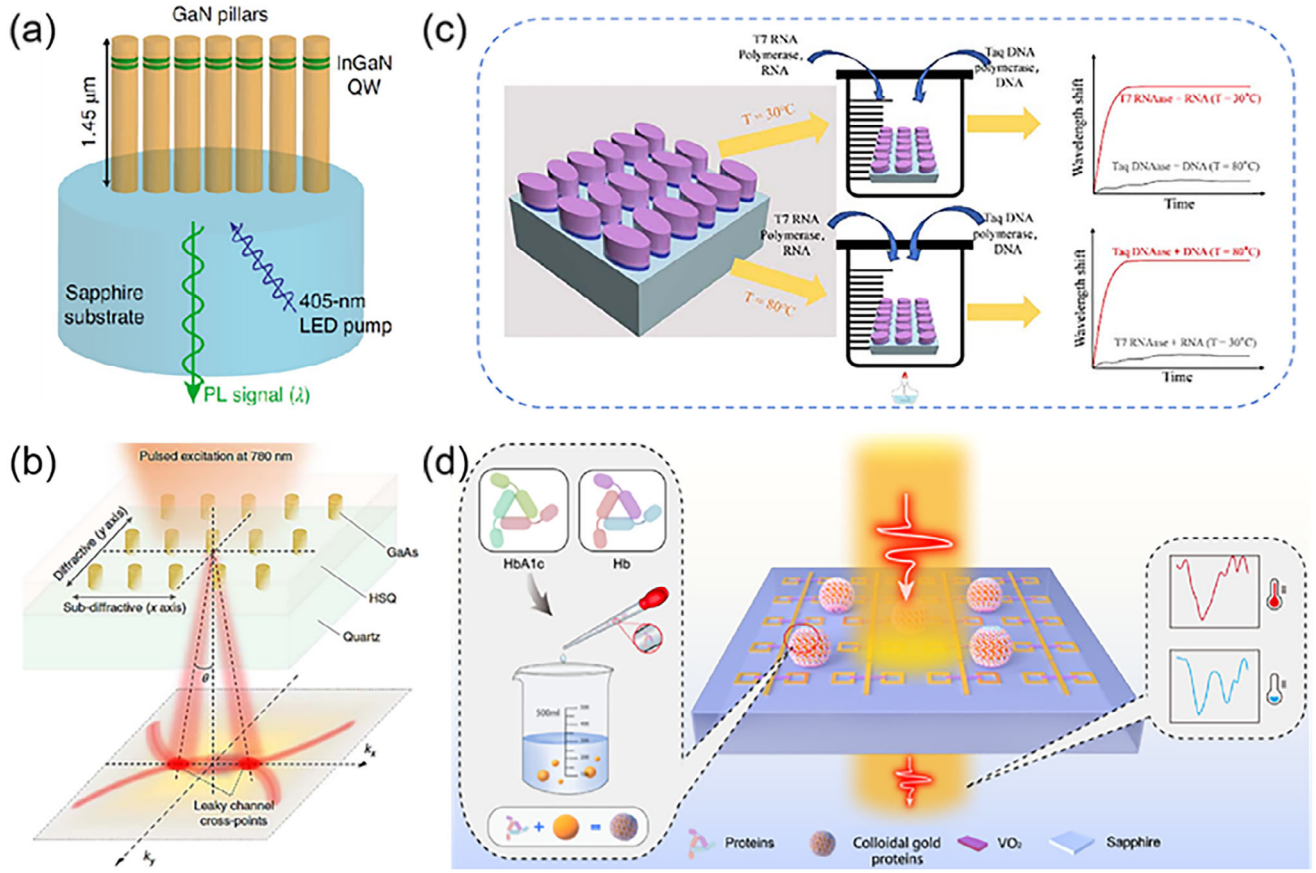

Figure 17. a) Unidirectional luminescence control of incoherent light sources with a 405 nm Light Emitting Diode (LED). Adapted with permission from ref. [191]. Copyright 2020, Nature Publishing Group. b) Schematic mechanism of compact surface-emitting laser based on nanoantenna. Adapted with permission from ref. [192]. Copyright 2018, Nature Publishing Group. c) The schematic diagram and experimental results of Si-VO_2 metasurface achieve multi-scene detection of biological enzymes through temperature regulation. Adapted with permission from ref. [194]. Copyright 2025, IOP Publishing. d) A VO_2-based tunable THz metasurface biosensor with dual-mode operation (EIT and Lorentz lattice modes). Adapted with permission from ref. [193]. Copyright 2025, American Chemical Society.

nanoscale. These engineered surfaces consist of subwavelength structures capable of dynamic modification to manipulate electromagnetic waves, enabling tunable optical properties such as phase, amplitude, and polarization.[188–190] This adaptability enhances the performance of optical devices and opens new avenues for innovative applications in biomedical diagnostics, environmental monitoring, and beyond. Building on this foundation, Iyer et al.[191] achieved narrowband, unidirectional transmission and photoluminescence beams by designing an InGaN/GaN quantum well metasurface. The emission angle could be flexibly controlled via the metasurface phase gradient. By varying nanopillar widths (150–210 nm), a linear phase gradient was created across the metasurface (**Figure 17a**), allowing flexible control of the emission angle (10°–80°). This design increased the total external quantum efficiency by seven times while improving polarization purity.

Furthermore, reconfigurable MDs based on dielectric nanoantennas can demonstrate singular laser emission. As shown in Figure 17b, combining the bound states in the continuum (BIC) concept with dielectric nanoantennas experimentally achieved low-threshold and highly directional laser emission. Structural design and temperature regulation demonstrated flexibility and adjustability in wavelength and angle, with high transparency exceeding 85%.[192] For example, THz biosensing was achieved by integrating dynamically reconfigurable VO_2 MDs, enabling dual-mode detection of ultralow-concentration biomolecules (Figure 17c).[193] By incorporating the BIC concept with VO_2 MDs, the biosensor operates at 30 °C (insulating state) and 80 °C (metallic state), adapting to the optimal reaction temperatures of various biological enzymes, such as Taq enzyme and T7 RNAse.[194] Enzyme activity is determined by shifts in the resonance peak at different temperatures.

In addition, Luo et al. established a foundational methodology for active photonic biosensors, with significant implications for diabetes monitoring, cancer biomarker detection, and real-time biofluid analysis, while providing a material roadmap for multifunctional metasurfaces in slow-light devices and adaptive optical computing architectures.[193] The sensor architecture consists of two rectangular SRR and a central cross-wire resonator, with a 100-nm VO_2 film strategically bridging the SRR gaps to enable thermal modulation of resonance coupling dynamics. Thermal actuation to 70 °C triggers VO_2's metallic phase transition,

suppressing the EIT window and shifting operational dominance to Lorentz lattice modes centered at 0.75 THz, thereby establishing a dual-state operational modality for cross-validated detection. Experimental validation demonstrates exceptional sensitivity metrics, achieving detection limits of 10 pM for hemoglobin and glycated hemoglobin through linear frequency shifts of 0.08 THz/RIU (EIT mode: from 0.6 to 0.58 THz) and 0.11 THz/RIU (Lorentz mode: from 0.75 to 0.72 THz) (Figure 17d). The VO_2 films exhibit optimized THz modulation depth of 45% at 0.7 THz and pattern fidelity, validated through optical microscopy and comparative performance analyses, surpassing conventional THz metasensors. However, challenges remain regarding operational thermal management and long-term VO_2 cyclability under repeated phase transitions, potentially addressable through tungsten doping or microfluidic integration for portable biosensing. To date, Yan et al.[195] also, compared the scattering patterns of a 10×10 array composed of unit cells operating in two distinct states, demonstrating potential applicability in multi-band THz frequency biological specimen detection.

5.4. Communication Technology

Currently, the integration of subwavelength meta-atoms with adaptive algorithms has enabled intelligent MDs to dynamically control electromagnetic wave propagation. This advancement addresses key challenges in spectral efficiency, hardware complexity, and energy consumption inherent in traditional 6G networks. For instance, Qian et al.[6] utilized both the Cascaded Single-Input Single-Output (SISO) channel model and the Sparse Angular Multiple-Input Multiple-Output (MIMO) channel model to simulate obstacle transmission in wireless communication (**Figure 18a**). They further suggested that expanding the operational frequency of MDs into millimeter waves and THz bands represents a future trend. However, this requires the development of new reconfigurable MDs. Additionally, PCMDs are regarded as promising candidates for achieving dynamic THz modulation due to their rapid response and wideband control capabilities, particularly in overcoming the bandwidth limitations of current components like PIN diodes. Moreover, Liu et al.[196] demonstrated a programmable diffractive deep neural network (D^2NN) based on a multi-layer digital-coding metadevice array, referred to as a Programmable Artificial Intelligence Machine (PAIM). As shown in Figure 18b, PAIM can accurately decode multiple user codes transmitted simultaneously, even in noisy environments (with an error rate of only 0.52%). This highlights its suitability for high-capacity communication scenarios. These MDs transcend fixed-function limitations by bridging physical wave dynamics with digital intelligence, offering transformative potential for adaptive wireless communications. Interestingly, the THz spectral range exhibits unique interactions with biological matter, such as exciting low-energy molecular vibrations, rotational modes of biomolecules, and enabling nonionizing penetration of soft tissues.

5.5. Medical Diagnosis

The characteristics position THz waves as a revolutionary tool for medical diagnostics, facilitating label-free, noninvasive interrogation of pathological states through molecular fingerprinting and dielectric contrast imaging.[197–199] Despite these advantages, significant challenges remain, including weak light-matter interactions at subwavelength scales, limited sensitivity for detecting trace biomarkers, and bulky configurations that hinder point-of-care applications. Recently, Liu et al.[200] introduced a novel nanoplasmonic microarray metadevice for real-time, label-free analysis of protein secretion dynamics in single tumoroids (Figure 18c). By combining optofluidic nanoplasmonic biosensors with a dual-layer microwell design, the platform enables simultaneous monitoring of secretion kinetics, morphology, and motility of tumoroids under varying conditions. The ultrasensitive medical diagnosis sensor achieves a detection limit of 157 pg mL^{-1} for vascular endothelial growth factor A (VEGF-A), allowing the detection of low-abundance biomarkers in small tumoroid populations. This innovation paves the way for more precise and efficient medical diagnostics.

To sum up, as shown in **Table 2**, the THz PCMDs display substantial modulation capabilities within both the THz and IR spectral ranges. Experimental results indicate that over 85% of the tested samples achieved modulation depths surpassing the 80% threshold. Compared to traditional PCM implementations in these frequency bands, the metamaterial-enhanced design offers three key advantages: stronger localization of electromagnetic fields for enhanced signal collection efficiency, superior modulation depth performance, and sub-millisecond temporal response times. Current challenges are primarily associated with the need for external energy inputs to induce phase transitions. This operational constraint calls for systematic optimization approaches, particularly through doping techniques and strategies to mitigate thermal degradation, which are essential for advancing the practical applicability of PCMDs. Future research should consider designing self-sustaining modulation systems via advanced material engineering and metastructure refinement.

6. Conclusion and Perspectives

Integrating phase-change materials (PCMs) with tunable and reconfigurable metasurfaces has sparked transformative advancements in terahertz (THz) photonics, enabling precise and dynamic manipulation of THz waves. This encompasses applications, such as THz wavefront modulation, adaptive control, and the seamless integration of multifunctional systems. This paper systematically reviews dynamic control mechanisms, structural designs, fabrication processes, and cutting-edge applications of four mainstream PCMs and their associated phase-change metasurfaces (PCMDs), with a focus on the phase transition characteristics and control methodologies of materials like vanadium dioxide (VO_2), germanium-antimony-tellurium (GST) alloys, strontium titanate (STO), and liquid crystals (LCs). VO_2 stands out for its ultrafast insulator-metal phase transition (IMPT) behavior, facilitating tunable THz absorption and polarization management.[35] Conversely, GST offers non-volatile amorphous-crystalline phase transition (ACPT) properties, ideal for programmable photonics and optical storage solutions. Furthermore, as a quantum paraelectric material, STO exhibits temperature-dependent dielectric tuning capabilities, enhancing its utility in adaptive resonance and slow-light devices.[205]

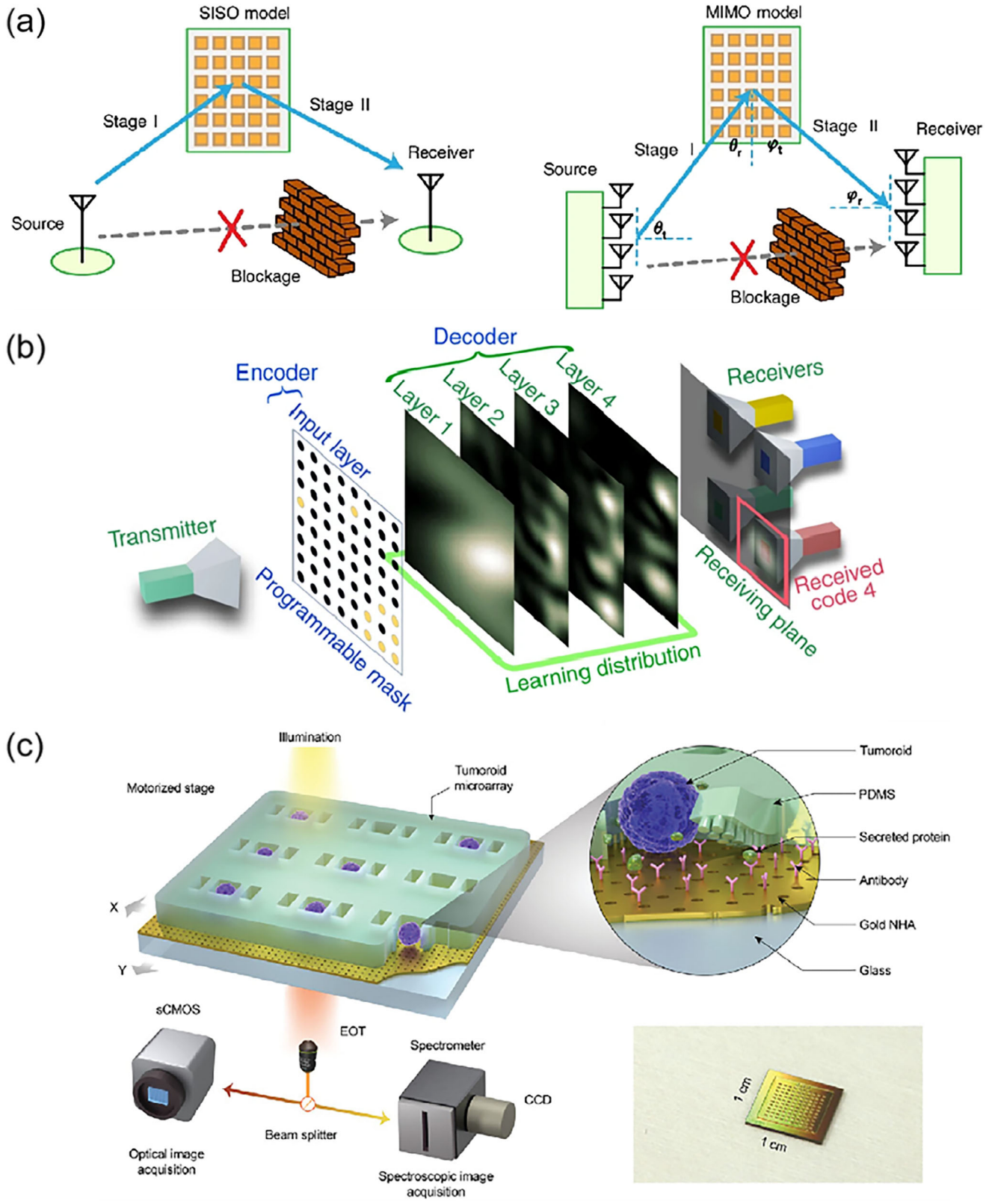

Figure 18. The fundamental principles and results in wireless communication and the Medical Diagnosis fields. a) The schematic diagram of how intelligent metasurface-assisted wireless communication technology works. Adapted with permission from ref. [6]. Copyright 2025, Nature Publishing Group. b) The schematic image of multi-user information dissemination. Adapted with permission from ref. [196]. Copyright 2022, Nature Publishing Group. c) The optical setup and detection principles of the nanoplasmonic biosensor platform. Adapted with permission from ref. [200]. Copyright 2024, Wiley.

Table 2. The performance comparison table for recently developed tunable/reconfigurable PCMDs used in THz regions.

PCMs	Modulation depth	Unit cell structures	External stimuli	Operation frequencies	Response time	Refs.
VO_2	99.9%	Feedback loop	Electrical (0–50 mA)	0.3–1.2 THz	≈1s	[201]
	83.4%	Gap = 5 μm	Thermal (80 °C)	0.65–0.75 THz	Slow	[202]
	90.5%	Ring	Thermal (77 °C)	2.64–7 THz	Slow	[203]
	80%	1550 nm/600 nm	Electrical (0–1.5 A)	2.5–5 μm	500 ms	[204]
GST	79%	Trapezoidal/cm	Voltage pulse (0–30 V)	0.3–1.5 THz	≈5 s	[123]
	85%	d = 15 μm	Optical (0–1250 μJ/cm^2)	0.5–1.2 THz	≈19 ps	[148]
STO	≈50%	4 μm/36 μm	Thermal (150–409 K)	0.1–0.3 THz	Slow	[126]
	34.4%/91.3%	SRR/8 μm gap	Electric field (0–33 kV/cm)	1.52–1.57 THz	N/A	[127]
	≈70%	2.5 × 3 mm^2 rods	Thermal (120–300 K)	0 – 0.42 THz	N/A	[103]
LC	13%/11%	Multifan blade	Voltage (0–50 V)	0.1 – 0.4 THz	≈0.02 s	[158]
	15%	Ring resonator	Voltage (0–45 V)	0.6 – 0.22 THz	≈100 ms	[118]

Advanced fabrication techniques, including atomic layer deposition (ALD), molecular beam epitaxy (MBE), lithography, and nanoimprinting, are employed to process complex PCMD architectures and integrate large-scale array systems. These methods enable functionalities such as dynamic imaging, biosensing, and multi-temporal programming. The interdisciplinary applications of these technologies span dynamic THz modulation (e.g., filters and absorbers), real-time image processing via in-sensor computing, and high-sensitivity biomolecular detection. Notably, certain frontier applications have garnered substantial academic interest; for instance, VO_2-based reconfigurable metasurfaces have been utilized for encoding and switchable holography,[206,207] showcasing their potential in advanced photonics and imaging technologies.

Despite significant progress, several challenges hinder broader implementation. The penetrative nature of THz waves results in insufficient coupling efficiency with PCMDs. Repeated phase transitions in these PCMs lead to cyclic fatigue, affecting operational lifespan. Due to soft phonon mode dynamics, bandwidth limitations in ferroelectric phase transition (FEPT) materials-based devices restrict their effectiveness in broadband applications. Additionally, there is a persistent trade-off between switching speed and energy efficiency. The scalability of these technologies poses integration difficulties with current semiconductor platforms, particularly for PCMDs with low-critical temperatures that require either cryogenic conditions or high electric fields. Overcoming these barriers necessitates multidisciplinary collaboration to refine material interfaces and optimize device architectures. The future development of tunable/reconfigurable THz PCMDs can proceed in the following directions:

6.1. Enhancing Intrinsic Capabilities of PCMs

Improving the intrinsic properties of PCMs is crucial for achieving more effective modulation outcomes. Techniques such as strain engineering and doping can enhance the THz modulation capability of PCMs, including sensitivity, response speed, and stability, while reducing energy consumption. For example, incorporating tungsten (W) or magnesium (Mg) into VO_2 can lower its phase transition temperature, boosting response speed and cycling stability. Strain modulation in FEPT heterostructures may increase dielectric tunability at room temperature, expanding potential applications. Additionally, fabricating PCM thin films on flexible substrates allows exploitation of substrate strain to enhance PCMD sensitivity, paving the way for developing wearable THz devices using reverse engineering principles.

6.2. Heterostructure Engineering for Multifunctionality

Heterostructure engineering facilitates the realization of multifunctionality or even multimodality in PCMDs. As miniaturization is a key trend for future THz devices, creating THz metasurfaces with integrated multifunctional capabilities is of substantial importance. By leveraging heterojunction engineering, it is possible to address intrinsic limitations of individual PCMs, such as volatility, low conductivity, and susceptibility to oxidation. This approach enables the fabrication of high-performance, multimodal THz heterostructure metasurfaces. For instance, hybrid architectures integrating VO_2's ultrafast switching characteristics with GST's non-volatility can open new avenues for dual-functional metasurfaces applicable to adaptive imaging and secure communication systems.

6.3. Improving CMOS-Compatible Processes

While various tunable/reconfigurable PCMDs based on distinct principles have been successfully developed, challenges remain in the patterning and etching of PCMs, with issues such as difficulty and limited precision persisting. The inadequate radiation and oxidation resistance of PCMs means exposure to acids, bases, and oxygen during photolithography and dry etching can significantly alter their phase-change characteristics, impacting device performance. Consequently, the performance of THz metasurfaces utilizing PCMs still has considerable potential for enhancement. Innovations in nanoimprint lithography and roll-to-roll processing will be crucial in establishing scalable, cost-efficient, low-temperature manufacturing techniques.

6.4. AI-Enabled Precise Design of PCMDs

Developing THz metasurfaces requires handling intricate electromagnetic modeling, computation, and simulation tasks, presenting substantial challenges in expertise and time investment. Utilizing advanced AI-driven tools (such as AI integrated with COMSOL Multiphysics or FDTD Solutions) alongside extensive research databases on PCMDs facilitates accurate structural design and optimization. This approach effectively resolves key issues like light-matter coupling efficiency, thermal interference between units, and optimal material selection for PCMDs. Incorporating an FPGA allows dynamic manipulation of THz waves and real-time switching among different functionalities by modifying the input coding sequence, significantly broadening the potential applications of PCMDs. Looking ahead, integrating sensors capable of monitoring factors such as temperature, humidity, and illumination could enhance PCMD's versatility and functionality, offering more pathways for advancing intelligent THz systems. Additionally, emerging domains like neuromorphic computing and quantum photonics hold great promise, particularly in utilizing the analog switching properties of reconfigurable metasurfaces to achieve energy-efficient data processing.

Acknowledgements

B.W.L. and J.C.L. contributed equally to this work. This work was financially supported in part by the Research Grants Council of the Hong Kong Special Administrative Region, China (Project No. CRS_CityU101/24), in part by the Science Technology and Innovation Committee of Shenzhen Municipality (Project No. JCYJ20230807114910021), and in part by Guangdong Basic and Applied Basic Research Fund (Project No. 2024A1515011922).

Conflict of Interest

The authors declare no conflict of interest.

Keywords

phase-change materials, reconfigurable metasurfaces, THz metadevices

Received: May 1, 2025
Revised: June 27, 2025
Published online:

[1] J. J. Hopfield, *Proc. Natl. Acad. Sci. USA* **1982**, *79*, 2554.
[2] Y. B. Yann LeCun, G. Hinton, *Nature* **2015**, *521*, 436.
[3] I. Rafiq, A. Mahmood, S. Razzaq, S. H. M. Jafri, I. Aziz, *J. Eng-Joe* **2023**, *2023*, e12262.
[4] A. Libanori, G. R. Chen, X. Zhao, Y. H. Zhou, J. Chen, *Nat. Electron.* **2022**, *5*, 142.
[5] N. Z. Laha Ale, S. A. King, D. Chen, *Nat. Rev. Electr. Eng.* **2024**, *1*, 478.
[6] C. Qian, L. Tian, H. Chen, *Light Sci. Appl.* **2025**, *14*, 93.
[7] R. Hillenbrand, Y. Abate, M. K. Liu, X. Z. Chen, D. N. Basov, *Nat. Rev. Mater.* **2025**, *10*, 285.
[8] Z. W. Jin, J. Lou, F. Z. Shu, Z. Hong, C. W. Qiu, *Research* **2025**, *8*, 0562.
[9] M. Tonouchi, *Nat. Photonics* **2007**, *1*, 97.
[10] M. Koch, D. M. Mittleman, J. Ornik, E. Castro-Camus, *Nat. Rev. Methods Prim.* **2023**, *3*, 48.
[11] X. Li, J. Li, Y. Li, A. Ozcan, M. Jarrahi, *Light Sci. Appl.* **2023**, *12*, 233.
[12] B. Ferguson, X. C. Zhang, *Nat. Mater.* **2002**, *1*, 26.
[13] Y. Liu, X. Zhang, *Chem. Soc. Rev.* **2011**, *40*, 2494.
[14] H. T. Chen, J. F. O'Hara, A. K. Azad, A. J. Taylor, *Laser Photonics Rev.* **2011**, *5*, 513.
[15] H. T. Chen, A. J. Taylor, N. F. Yu, *Rep. Prog. Phys.* **2016**, *79*, 076401.
[16] M. Seo, J. Kyoung, H. Park, S. Koo, H. S. Kim, H. Bernien, B. J. Kim, J. H. Choe, Y. H. Ahn, H. T. Kim, N. Park, Q. H. Park, K. Ahn, D. S. Kim, *Nano Lett.* **2010**, *10*, 2064.
[17] F. Lu, H. Ou, Y. S. Lin, *Opt. Lett.* **2020**, *45*, 6482.
[18] D. Wang, K. D. Xu, S. Luo, Y. Cui, L. Zhang, J. Cui, *Nanoscale* **2023**, *15*, 3398.
[19] A. Maleki, A. Singh, A. Jaber, W. Cui, Y. B. Xin, B. T. Sullivan, R. W. Boyd, J. M. Ménard, *Photonics Res.* **2023**, *11*, 526.
[20] W. J. Wang, K. X. Sun, Y. Xue, J. Lin, J. K. Fang, S. N. Shi, S. Zhang, Y. P. Shi, *Opt. Commun.* **2024**, *556*, 130266.
[21] S. Karmakar, D. Kumar, R. K. Varshney, D. R. Chowdhury, *J. Phys. D Appl. Phys.* **2020**, *53*, 415101.
[22] K. Sengupta, T. Nagatsuma, D. M. Mittleman, *Nat. Electron.* **2018**, *1*, 622.
[23] J. C. Wang, I. Harris, M. Ibrahim, D. Englund, R. N. Han, *Nat. Electron.* **2025**, *1*.
[24] J. N. Li, J. Y. Chen, D. X. Yan, F. Fan, K. Chen, K. Zhong, Y. Y. Wang, Z. Tian, D. G. Xu, *Adv. Photon. Res.* **2024**, *5*.
[25] C. Jung, E. Lee, J. Rho, *Sci. Adv* **2024**, *10*, ado8964.
[26] W. Wang, Y. J. Tan, T. C. Tan, A. Kumar, P. Pitchappa, P. Szriftgiser, G. Ducournau, R. Singh, *Nature* **2024**, *632*, 522.
[27] M. Samizadeh Nikoo, E. Matioli, *Nature* **2023**, *614*, 451.
[28] W. He, X. Cheng, S. Hu, Z. Ren, Z. Yu, S. Wan, Y. Hu, T. Jiang, *Light Sci. Appl.* **2024**, *13*, 142.
[29] L. Cong, Y. K. Srivastava, H. Zhang, X. Zhang, J. Han, R. Singh, *Light Sci. Appl.* **2018**, *7*, 28.
[30] C. Bortolotti, F. Grandi, M. Butti, L. Gatto, F. Modena, C. Kousseff, I. McCulloch, C. Vozzi, M. Caironi, E. Cinquanta, G. E. Bonacchini, *Nat. Commun.* **2024**, *15*, 9639.
[31] Z. Chen, X. Chen, L. Tao, K. Chen, M. Long, X. Liu, K. Yan, R. I. Stantchev, E. Pickwell-MacPherson, J. B. Xu, *Nat. Commun.* **2018**, *9*, 4909.
[32] W. Y. Kim, H. D. Kim, T. T. Kim, H. S. Park, K. Lee, H. J. Choi, S. H. Lee, J. Son, N. Park, B. Min, *Nat. Commun.* **2016**, *7*, 10429.
[33] F. J. Zhu, K. N. Yang, J. H. Hao, K. B. Fan, H. Ma, J. B. Wu, C. H. Zhang, X. P. Zhang, H. B. Wang, B. B. Jin, J. Chen, P. H. Wu, *Laser Photonics Rev.* **2025**, *19*, 2401732.
[34] W. Li, B. Chen, X. Hu, H. Guo, S. Wang, J. Wu, K. Fan, C. Zhang, H. Wang, B. Jin, J. Chen, P. Wu, *Sci. Adv.* **2023**, *9*, adi7565.
[35] B. Chen, X. Wang, W. Li, C. Li, Z. Wang, H. Guo, J. Wu, K. Fan, C. Zhang, Y. He, B. Jin, J. Chen, P. Wu, *Sci. Adv.* **2022**, *8*, add1296.
[36] X. Y. Chen, S. J. Zhang, K. Liu, H. Y. Li, Y. H. Xu, J. J. Chen, Y. C. Lu, Q. W. Wang, X. Feng, K. M. Wang, Z. R. Liu, T. Cao, Z. Tian, *ACS Photonics* **2022**, *9*, 1638.
[37] H. X. Zeng, X. Cong, H. F. Zhang, S. Gong, T. C. Zhou, L. Wang, H. Y. Cao, H. J. Liang, S. X. Liang, S. Q. Wang, F. Lan, X. Wang, Z. Q. Yang, Y. X. Zhang, T. J. Cui, *Sci. Adv.* **2024**, *10*, eadr1448.
[38] L. K. Piper, H. J. Singh, J. R. C. Woods, K. Sun, O. L. Muskens, V. Apostolopoulos, *Adv. Photon. Res.* **2021**, *2*, 2100136.
[39] Z. L. Yinghao Zhao, C. Li, W. Jiao, S. Jiang, X. Li, J. Duan, J. Li, *npj Nanophotonics* **2024**, *1*, 16.
[40] S. Y. Long, W. Zhang, Z. Q. Xue, G. Z. Xu, P. P. Shum, D. Luo, L. Q. Cong, *Laser Photonics Rev.* **2025**, 2402167.
[41] X. Lu, F. Zhang, L. Zhu, S. Peng, J. Yan, Q. Shi, K. Chen, X. Chang, H. Zhu, C. Zhang, W. Huang, Q. Cheng, *Nat. Commun.* **2024**, *15*, 3157.

[42] R. Degl'Innocenti, H. Lin, M. Navarro-Cia, *Nanophotonics* **2022**, *11*, 1485.
[43] S. Nourinovin, M. Navarro-Cía, M. M. Rahman, M. P. Philpott, Q. H. Abbasi, A. Alomainy, *IEEE Antennas Propag. Mag.* **2022**, *64*, 60.
[44] R. Ulrich, *Infrared Phys* **1967**, *7*, 37.
[45] C. S. R. Kaipa, A. B. Yakovlev, F. Medina, F. Mesa, *J. Appl. Phys.* **2012**, *112*, 033101.
[46] Y. C. Chung, K. W. Lee, I. P. Hong, M. G. Lee, H. J. Chun, J. G. Yook, *IEICE Electron. Expr.* **2011**, *8*, 89.
[47] Y. R. Padooru, A. B. Yakovlev, C. S. R. Kaipa, F. Medina, F. Mesa, *Phys. Rev. B* **2011**, *84*, 035108.
[48] O. Luukkonen, C. Simovski, G. Granet, G. Goussetis, D. Lioubtchenko, A. V. Räisänen, S. A. Tretyakov, *IEEE Trans. Antennas and Propag.* **2008**, *56*, 1624.
[49] F. Falcone, T. Lopetegi, M. A. Laso, J. D. Baena, J. Bonache, M. Beruete, R. Marques, F. Martin, M. Sorolla, *Phys. Rev. Lett.* **2004**, *93*, 197401.
[50] A. Bitzer, A. Ortner, H. Merbold, T. Feurer, M. Walther, *Opt. Express* **2011**, *19*, 2537.
[51] M. Zalkovskij, R. Malureanu, C. Kremers, D. N. Chigrin, A. Novitsky, S. Zhukovsky, P. T. Tang, P. U. Jepsen, A. V. Lavrinenko, *Laser Photonics Rev.* **2013**, *7*, 810.
[52] M. Walther, D. G. Cooke, C. Sherstan, M. Hajar, M. R. Freeman, F. A. Hegmann, *Phys. Rev. B* **2007**, *76*, 125408.
[53] D. X. Zhou, E. P. J. Parrott, D. J. Paul, J. A. Zeitler, *J. Appl. Phys.* **2008**, *104*, 093530.
[54] J. Huang, J. Li, Y. Yang, J. Li, J. Li, Y. Zhang, J. Yao, *Opt. Express* **2020**, *28*, 17832.
[55] W. Li, M. Xu, H. X. Xu, X. Wang, W. Huang, *Adv. Mater.* **2022**, *34*, 2202509.
[56] L. B. Zhang, P. H. Zhou, H. Y. Chen, H. P. Lu, J. L. Xie, L. J. Deng, *Appl. Phys. A-Mater.* **2015**, *121*, 233.
[57] S. J. Zhang, B. Cheng, Z. G. Gao, D. Lan, Z. W. Zhao, F. C. Wei, Q. S. Zhu, X. P. Lu, G. L. Wu, *J. Alloy. Compd.* **2022**, *893*, 162343.
[58] Z. C. Zhai, L. Zhang, X. J. Li, S. S. Xiao, *Opt. Commun.* **2019**, *431*, 199.
[59] M. D. Zou, Y. Li, W. Q. Zhao, X. Zhang, Y. D. Wu, C. Peng, L. N. Fan, J. X. Li, J. Y. Yan, J. Q. Zhuang, J. C. Mei, X. P. Wang, *Opt. Eng.* **2021**, *60*, 087103.
[60] T. L. Wu, W. Li, S. W. Chen, J. G. Guan, *Results Phys* **2021**, *20*, 103753.
[61] F. J. Morin, *Phys. Rev. Lett.* **1959**, *3*, 34.
[62] S. Westman, I. Lindqvist, B. Sparrman, G. B. Nielsen, H. Nord, A. Jart, *Acta Chem. Scand. (1989)* **1961**, *15*, 217.
[63] B. W. Li, L. Y. Xie, Z. W. Wang, S. Chen, H. Ren, Y. L. Chen, C. M. Wang, G. B. Zhang, J. Jiang, C. W. Zou, *Angew. Chem., Int. Ed.* **2019**, *58*, 13711.
[64] Y. Wu, W. Tao, F. Zhao, C. Li, B. Fang, P. Zhang, Z. Hong, X. Jing, M. Yu, *Opt. Laser Technol.* **2024**, *179*, 111376.
[65] Z. Li, J. Wu, Z. Hu, Y. Lin, Q. Chen, Y. Guo, Y. Liu, Y. Zhao, J. Peng, W. Chu, C. Wu, Y. Xie, *Nat. Commun.* **2017**, *8*, 15561.
[66] B. Li, P. Xie, B. Chen, Y. Meng, W. Wang, M. Yang, B. Gao, Q. Quan, Y. Yan, M. Ding, D. Li, C. H. Chan, J. C. Ho, *Adv. Mater.* **2024**, *36*, 2410952.
[67] B. Li, N. Lin, Z. Wang, B. Chen, C. Lan, X. Li, Y. Meng, W. Wang, M. Ding, P. Xie, Y. Zhang, Z. Wu, D. Li, F. R. Chen, C. H. Chan, Z. Wang, J. C. Ho, *Adv. Mater.* **2025**, 2502915.
[68] X. Ao, B. Li, B. Zhao, M. Hu, H. Ren, H. Yang, J. Liu, J. Cao, J. Feng, Y. Yang, Z. Qi, L. Li, C. Zou, G. Pei, *Proc. Natl. Acad. Sci. USA* **2022**, *119*, 2120557119.
[69] C. Feng, B. W. Li, Y. Dong, X. D. Chen, Y. Zheng, Z. H. Wang, H. B. Lin, W. Jiang, S. C. Zhang, C. W. Zou, G. C. Guo, F. W. Sun, *Sci. Adv.* **2023**, *9*, adg9376.
[70] T. Yao, X. Zhang, Z. Sun, S. Liu, Y. Huang, Y. Xie, C. Wu, X. Yuan, W. Zhang, Z. Wu, G. Pan, F. Hu, L. Wu, Q. Liu, S. Wei, *Phys. Rev. Lett.* **2010**, *105*, 226405.
[71] F.-W. Guo, W.-H. Liu, Z. Wang, S.-S. Li, L.-W. Wang, J.-W. Luo, *Nat. Commun.* **2025**, *16*, 94.
[72] T. Siegrist, P. Jost, H. Volker, M. Woda, P. Merkelbach, C. Schlockermann, M. Wuttig, *Nat. Mater.* **2011**, *10*, 202.
[73] D. Loke, T. H. Lee, W. J. Wang, L. P. Shi, R. Zhao, Y. C. Yeo, T. C. Chong, S. R. Elliott, *Science* **2012**, *336*, 1566.
[74] C. Ríos, M. Stegmaier, P. Hosseini, D. Wang, T. Scherer, C. D. Wright, H. Bhaskaran, W. H. P. Pernice, *Nat. Photonics* **2015**, *9*, 725.
[75] K. Shportko, S. Kremers, M. Woda, D. Lencer, J. Robertson, M. Wuttig, *Nat. Mater.* **2008**, *7*, 653.
[76] N. Yamada, E. Ohno, K. Nishiuchi, N. Akahira, M. Takao, *J.Appl. Phys.* **1991**, *69*, 2849.
[77] V. Bragaglia, F. Arciprete, W. Zhang, A. M. Mio, E. Zallo, K. Perumal, A. Giussani, S. Cecchi, J. E. Boschker, H. Riechert, S. Privitera, E. Rimini, R. Mazzarello, R. Calarco, *Sci. Rep.* **2016**, *6*, 23843.
[78] E. Morales-Sánchez, E. F. Prokhorov, J. González-Hernández, A. Mendoza-Galván, *Thin Solid Films* **2005**, *471*, 243.
[79] S. Ran, E. Petroni, L. Laurin, M. Baldo, A. Serafini, M.-A. Luong, A. Motta, A. Redaelli, A. Claverie, *Sci. Rep.* **2025**, *15*, 11357.
[80] K. Aryana, J. T. Gaskins, J. Nag, D. A. Stewart, Z. Bai, S. Mukhopadhyay, J. C. Read, D. H. Olson, E. R. Hoglund, J. M. Howe, A. Giri, M. K. Grobis, P. E. Hopkins, *Nat. Commun.* **2021**, *12*, 774.
[81] H. Lv, P. Zhou, Y. Lin, T. Tang, B. Qiao, Y. Lai, J. Feng, B. Cai, B. Chen, *Microelectron. J* **2006**, *37*, 982.
[82] A. A. Nevzorov, V. A. Mikhalevsky, A. V. Kiselev, A. A. Burtsev, N. N. Eliseev, V. V. Ionin, A. A. Lotin, *Opt. Mater.* **2023**, *141*, 113925.
[83] C. Li, S. Du, R. Pan, X. Xiong, Z. Tang, R. Zheng, Y. Liu, G. Geng, J. Sun, C. Gu, H. Guo, J. Li, *Adv. Funct. Mater.* **2024**, *34*, 2470078.
[84] C. H. Kodama, R. A. Coutu, Jr., *Appl. Phys. Lett.* **2016**, *108*, 231901.
[85] H. Hirori, A. Doi, F. Blanchard, K. Tanaka, *Appl. Phys. Lett.* **2011**, *98*, 091106.
[86] P. Pitchappa, A. Kumar, S. Prakash, H. Jani, R. Medwal, M. Mishra, R. S. Rawat, T. Venkatesan, N. Wang, R. Singh, *Adv. Funct. Mater.* **2021**, *31*, 2100200.
[87] Y. Sanari, T. Tachizaki, Y. Saito, K. Makino, P. Fons, A. V. Kolobov, J. Tominaga, K. Tanaka, Y. Kanemitsu, M. Hase, H. Hirori, *Phys. Rev. Lett.* **2018**, *121*, 165702.
[88] P. Zalden, M. J. Shu, F. Chen, X. Wu, Y. Zhu, H. Wen, S. Johnston, Z.-X. Shen, P. Landreman, M. Brongersma, S. W. Fong, H. S. P. Wong, M.-J. Sher, P. Jost, M. Kaes, M. Salinga, A. von Hoegen, M. Wuttig, A. M. Lindenberg, *Phys. Rev. Lett.* **2016**, *117*, 067601.
[89] Y.-G. Jeong, Y.-M. Bahk, D.-S. Kim, *Adv. Opt. Mater.* **2020**, *8*, 1900548.
[90] A. A. Sirenko, C. Bernhard, A. Golnik, A. M. Clark, J. Hao, W. Si, X. X. Xi, *Nature* **2000**, *404*, 373.
[91] J. Petzelt, T. Ostapchuk, I. Gregora, I. Rychetský, S. Hoffmann-Eifert, A. V. Pronin, Y. Yuzyuk, B. P. Gorshunov, S. Kamba, V. Bovtun, J. Pokorný, M. Savinov, V. Porokhonskyy, D. Rafaja, P. Vaněk, A. Almeida, M. R. Chaves, A. A. Volkov, M. Dressel, R. Waser, *Phys. Rev. B* **2001**, *64*, 184111.
[92] H. Köppel, H. Barentzen, *Jahn-Teller Effect: Fundament. Impl. Phys. Chem.* **2009**, *97*, 3.
[93] J. Mannhart, D. G. Schlom, *Nature* **2004**, *430*, 620.
[94] K. Shirai, K. Yamanaka, *J. Appl. Phys.* **2013**, *113*, 053705.
[95] P. A. Fleury, J. M. Worlock, *Phys. Rev.* **1968**, *174*, 613.
[96] Y. Yamada, G. Shirane, *J. Phys. Soc. Jpn* **1969**, *26*, 396.
[97] A. Yamanaka, M. Kataoka, Y. Inaba, K. Inoue, B. Hehlen, E. Courtens, *Europhys. Lett.* **2000**, *50*, 688.
[98] J. Petzelt, P. Kužel, I. Rychetský, A. Pashkin, T. Ostapchuk, *Ferroelect.* **2003**, *288*, 169.
[99] M. Misra, K. Kotani, I. Kawayama, H. Murakami, M. Tonouchi, *Appl. Phys. Lett.* **2005**, *87*, 182909.
[100] O. Buchnev, J. Y. Ou, M. Kaczmarek, N. I. Zheludev, V. A. Fedotov, *Opt. Express* **2013**, *21*, 1633.
[101] M. Asif, A. Afaq, M. Amin, K. Raouf, A. Majeed, M. Asif, *Mater. Today Commun* **2023**, *37*, 106966.

[102] M. Basletic, J. L. Maurice, C. Carrétéro, G. Herranz, O. Copie, M. Bibes, É. Jacquet, K. Bouzehouane, S. Fusil, A. Barthélémy, *Nat. Mater.* **2008**, *7*, 621.
[103] H. Němec, P. Kužel, F. Kadlec, C. Kadlec, R. Yahiaoui, P. Mounaix, *Phys. Rev. B* **2009**, *79*, 241108.
[104] I.-C. Khoo, *Liquid crystals*, John Wiley & Sons, Hoboken, NJ, **2022**.
[105] W. Zou, C. Zhong, L. Hong, J. Lei, Y. Shen, X. Deng, J. Chen, T. Guo, *Micromachines* **2024**, *15*, 967.
[106] F. C. Frank, *Discuss. Faraday Soc.* **1958**, *25*, 19.
[107] P.-G. De Gennes, J. Prost, *The physics of liquid crystals*, Oxford University Press, Oxford, United Kingdom, **1993**.
[108] K. Binnemans, *Chem. Rev.* **2005**, *105*, 4148.
[109] C. Oseen, *Trans. Faraday Soc.* **1933**, *29*, 883.
[110] M. Chen, M. Gao, L. Bai, H. Zheng, H. J. Qi, K. Zhou, *Adv. Mater.* **2023**, *35*, 2209566.
[111] L. Wang, Y. Wang, G. Zong, W. Hu, Y. Lu, *J. Materiomics* **2025**, *11*, 100888.
[112] X. Zhuang, W. Zhang, K. Wang, Y. Gu, Y. An, X. Zhang, J. Gu, D. Luo, J. Han, W. Zhang, *Light: Sci. Appl.* **2023**, *12*, 14.
[113] X. Fu, L. Shi, J. Yang, Y. Fu, C. Liu, J. W. Wu, F. Yang, L. Bao, T. J. Cui, *ACS Appl. Mater. Interfaces* **2022**, *14*, 22287.
[114] N. Vieweg, M. K. Shakfa, B. Scherger, M. Mikulics, M. Koch, *J. Infrared, Millim. & Terahertz Waves* **2010**, *31*, 1312.
[115] S. Savo, D. Shrekenhamer, W. J. Padilla, *Adv. Opt. Mater.* **2014**, *2*, 275.
[116] W. Meng, Y. Gao, X. Hu, L. Tan, L. Li, G. Zhou, H. Yang, J. Wang, L. Jiang, *ACS Appl. Mater. Interfaces* **2022**, *14*, 28301.
[117] H. Park, E. P. J. Parrott, F. Fan, M. Lim, H. Han, V. G. Chigrinov, E. Pickwell-MacPherson, *Opt. Express* **2012**, *20*, 11899.
[118] Z. Shen, S. Zhou, S. Ge, W. Duan, P. Chen, L. Wang, W. Hu, Y. Lu, *Opt. Lett.* **2018**, *43*, 4695.
[119] R. Zhou, T. Jiang, Z. Peng, Z. Li, M. Zhang, S. Wang, L. Li, H. Liang, S. Ruan, H. Su, *Opt. Mater.* **2021**, *114*, 110915.
[120] X. Lian, M. Ma, J. Tian, R. Yang, *Diam. Relat. Mater.* **2023**, *136*, 110060.
[121] M. Hasankhani, H. Vahed, M. Bemani, *Opt. Commun.* **2024**, *562*, 130567.
[122] C. Li, Z. Song, *Opt. Laser Technol.* **2023**, *157*, 108764.
[123] X. Chen, S. Zhang, K. Liu, H. Li, Y. Xu, J. Chen, Y. Lu, Q. Wang, X. Feng, K. Wang, Z. Liu, T. Cao, Z. Tian, *ACS Photonics* **2022**, *9*, 1638.
[124] K. Zhou, J. Nan, J. Shen, Z. Li, J. C. Cao, Z. Song, M. Zhu, B. He, M. Yan, H. Zeng, H. Li, *APL Mater.* **2021**, *9*.
[125] A. A. Gavdush, G. A. Komandin, V. V. Bukin, K. I. Zaytsev, D. S. Ponomarev, L. Tan, W. Huang, Q. Shi, *J. Appl. Phys.* **2023**, *134*, 085103.
[126] R. Singh, A. K. Azad, Q. X. Jia, A. J. Taylor, H.-T. Chen, *Opt. Lett.* **2011**, *36*, 1230.
[127] Y. Bian, C. Wu, H. Li, J. Zhai, *Appl. Phys. Lett.* **2014**, *104*, 251115.
[128] W. Li, Y. Cheng, *Opt. Commun.* **2020**, *462*, 125265.
[129] D.-K. Yang, S.-T. Wu, *Fundamentals of liquid crystal devices*, John Wiley & Sons, Hoboken, New Jersey, **2014**.
[130] S. K. Prasad, K. L. Sandhya, G. G. Nair, U. S. Hiremath, C. V. Yelamaggad, S. Sampath, *Liq. Cryst.* **2006**, *33*, 1121.
[131] D. Yang, W. Wang, E. Lv, H. Wang, B. Liu, Y. Hou, J.-h. Chen, *iScience* **2022**, *25*, 104824.
[132] M. Liu, X. Li, W. Zhang, L. Li, L. Li, C. Wang, G. Pei, B. Zhao, C. Zou, *Adv. Sci.* **2025**, *12*, 2416688.
[133] A. V. Ivanov, A. Y. Tatarenko, A. A. Gorodetsky, O. N. Makarevich, M. Navarro-Cía, A. M. Makarevich, A. R. Kaul, A. A. Eliseev, O. V. Boytsova, *ACS Appl. Nano Mater* **2021**, *4*, 10592.
[134] J. Ma, T. Kang, Z. Ke, M. Yao, X. Ma, Q. Luo, L. Bi, J. Qin, *Adv. Opt. Mater* **2024**, *12*, 2302390.
[135] C. Fu, X. Wang, Y. Zhang, J. Ju, W. Fan, X. Yan, L. Han, *Dalton T* **2024**, *54*, 133.
[136] W. Dong, L. Yang, B. Cai, L. Wu, Y. Cheng, F. Chen, H. Luo, X. Li, *J. Phys. D: Appl. Phys.* **2024**, *58*, 035106.
[137] D. J. Park, J. H. Shin, K. H. Park, H. C. Ryu, *Opt. Express* **2018**, *26*, 17397.
[138] Y. G. Jeong, S. Han, J. Rhie, J. S. Kyoung, J. W. Choi, N. Park, S. Hong, B. J. Kim, H. T. Kim, D. S. Kim, *Nano Lett.* **2015**, *15*, 6318.
[139] M. Liu, H. Y. Hwang, H. Tao, A. C. Strikwerda, K. Fan, G. R. Keiser, A. J. Sternbach, K. G. West, S. Kittiwatanakul, J. Lu, S. A. Wolf, F. G. Omenetto, X. Zhang, K. A. Nelson, R. D. Averitt, *Nature* **2012**, *487*, 345.
[140] D. Meng, M. N. F. Hoque, W. Wang, F. Zhaoyang, K. Wang, J. Lai, C. Chen, *Opt. Lett.* **2015**, *40*, 1745.
[141] Q.-Y. Wen, H.-W. Zhang, Y.-S. Xie, Q.-H. Yang, Y.-L. Liu, *Appl. Phys. Lett.* **2009**, *95*, 241111.
[142] S. Zhao, L. Li, C. Hu, B. Li, M. Liu, J. Zhu, T. Zhou, W. Shi, C. Zou, *Adv. Sci.* **2023**, *10*, 2300908.
[143] B. W. Li, Z. W. Wang, S. G. Zhao, C. L. Hu, L. Li, M. L. Liu, J. L. Zhu, T. Zhou, G. B. Zhang, J. Jiang, C. W. Zou, *Small Methods* **2022**, *6*, 2200931.
[144] Z. J. Thompson, A. Stickel, Y.-G. Jeong, S. Han, B. H. Son, M. J. Paul, B. Lee, A. Mousavian, G. Seo, H.-T. Kim, Y.-S. Lee, D.-S. Kim, *Nano Lett.* **2015**, *15*, 5893.
[145] A. X. Gray, M. C. Hoffmann, J. Jeong, N. P. Aetukuri, D. Zhu, H. Y. Hwang, N. C. Brandt, H. Wen, A. J. Sternbach, S. Bonetti, A. H. Reid, R. Kukreja, C. Graves, T. Wang, P. Granitzka, Z. Chen, D. J. Higley, T. Chase, E. Jal, E. Abreu, M. K. Liu, T. C. Weng, D. Sokaras, D. Nordlund, M. Chollet, R. Alonso-Mori, H. Lemke, J. M. Glownia, M. Trigo, Y. Zhu, et al., *Phys. Rev. B* **2018**, *98*, 045104.
[146] C. Li, S. Du, R. Pan, X. Xiong, Z. Tang, R. Zheng, Y. Liu, G. Geng, J. Sun, C. Gu, *Adv. Funct. Mater.* **2024**, *34*, 2310626.
[147] C. Kodama, J. R. Coutu, *Appl. Phys. Lett.* **2016**, *108*, 231901.
[148] P. Pitchappa, A. Kumar, S. Prakash, H. Jani, T. Venkatesan, R. Singh, *Adv. Mater.* **2019**, *31*, 1808157.
[149] Z. Zhao, F. Yu, J. Chen, X. Li, J. Wang, G. Li, X. Chen, W. Lu, *Opt. Commun.* **2025**, *576*, 131322.
[150] C. Choi, S.-E. Mun, J. Sung, K. Choi, S.-Y. Lee, B. Lee, *Adv. Funct. Mater.* **2021**, *31*, 2007210.
[151] S. Abdollahramezani, O. Hemmatyar, M. Taghinejad, H. Taghinejad, A. Krasnok, A. A. Eftekhar, C. Teichrib, S. Deshmukh, M. A. El-Sayed, E. Pop, M. Wuttig, A. Alù, W. Cai, A. Adibi, *Nat. Commun.* **2022**, *13*, 1696.
[152] G. Wang, C. Liu, W. Guo, X. Huang, Y. Jia, J. Liu, Z. Li, L. Li, H. Tian, *Opt. Laser Technol.* **2025**, *181*, 111556.
[153] Y. Zhang, X. Zhang, Z. Li, L. Liang, X. Yan, H. Yao, Z. Wang, X. Hu, Z. Shi, F. Huai, J. Wu, Q. Wang, Y. Chen, *Phys. Scr.* **2025**, *100*, 035548.
[154] L. Wu, T. Du, N. Xu, C. Ding, H. Li, Q. Sheng, M. Liu, J. Yao, Z. Wang, X. Lou, W. Zhang, *Small* **2016**, *12*, 2610.
[155] H. Zeng, S. Gong, L. Wang, T. Zhou, Y. Zhang, F. Lan, X. Cong, L. Wang, T. Song, Y. Zhao, Z. Yang, D. M. Mittleman, *Nanophotonics* **2022**, *11*, 415.
[156] J. Wang, H. Tian, Y. Wang, X. Li, Y. Cao, L. Li, J. Liu, Z. Zhou, *Opt. Express* **2018**, *26*, 5769.
[157] X. Chen, K. Li, R. Zhang, S. K. Gupta, A. K. Srivastava, E. Pickwell-MacPherson, *Adv. Opt. Mater.* **2019**, *7*, 1901321.
[158] Y. Hao, Z. Niu, J. Yang, M. Wang, H. Liu, Y. Qin, W. Su, H. Zhang, C. Zhang, X. Li, *ACS Appl. Mater. Interfaces* **2024**, *16*, 32249.
[159] L. Wang, S. Ge, W. Hu, M. Nakajima, Y. Lu, *Opt. Express* **2017**, *25*, 23873.
[160] D. C. Zografopoulos, R. Beccherelli, *Sci. Rep.* **2015**, *5*, 13137.
[161] L.-H. Jiang, F. Wang, R. Liang, Z. Wei, H. Meng, H. Dong, H. Cen, L. Wang, S. Qin, *Plasmonics* **2018**, *13*, 525.
[162] S. Guo, C. Hu, H. Zhang, *J. Opt. Soc. Am. B* **2020**, *37*, 2678.
[163] C. Rong, B. Cai, Y. Cheng, F. Chen, H. Luo, X. Li, *Phys. Chem. Chem. Phys.* **2024**, *26*, 5579.

[164] S. Liao, J. Sui, H. Zhang, *Opt. Express* **2022**, *30*, 34172.
[165] J. Qu, H. Pan, Y. Z. Sun, H. F. Zhang, *Ann. Phys.* **2022**, *534*, 2200175.
[166] W. Lu, Z. Yi, J. Zhang, X. Xu, B. Tang, G. Li, L. Zeng, J. Chen, T. Sun, *Diam. Relat. Mater.* **2023**, *140*, 110481.
[167] J. W. Zhang, Z. J. Qi, L. J. Wu, Q. Y. Zhou, J. Y. Dai, W. W. Cao, X. Ge, C. L. Gao, X. Gao, S. R. Wang, Z. X. Wang, L. F. Yao, J. W. Wu, J. N. Zhang, T. J. Cui, Q. Cheng, *Natl. Sci. Rev.* **2025**, *12*, nwaf017.
[168] Y. Ke, Y. Yin, Q. Zhang, Y. Tan, P. Hu, S. Wang, Y. Tang, Y. Zhou, X. Wen, S. Wu, T. J. White, J. Yin, J. Peng, Q. Xiong, D. Zhao, Y. Long, *Joule* **2019**, *3*, 858.
[169] L. Wang, Z. Li, C. Cao, J. Yang, C. Yang, X. Cao, *Chem. Eng. J.* **2024**, *488*, 150972.
[170] S. Hwang, Y. Hwang, B. Park, J. Ah Lee, D.-H. Choi, A. Ra Kim, S.-K. Lee, J.-D. Kwon, S.-H. Kwon, Y. Kim, *Appl. Surf. Sci.* **2022**, *604*, 154523.
[171] Z. Li, S. Zhao, Z. Shao, H. Jia, A. Huang, P. Jin, X. Cao, *Chem. Eng. J.* **2022**, *447*, 137556.
[172] Y. Malevich, M. S. Ergoktas, G. Bakan, P. Steiner, C. Kocabas, *Nat. Commun.* **2025**, *16*, 2907.
[173] D. Wang, B. Cai, L. Yang, L. Wu, Y. Cheng, F. Chen, H. Luo, X. Li, *Surf. Interfaces* **2024**, *49*, 104403.
[174] Y. He, B. Cai, L. Wu, L. Chen, Y. Cheng, F. Chen, H. Luo, X. Li, *Phys. Rev. B* **2024**, *681*, 415848.
[175] W. Wu, *Opt. Continuum.* **2025**, *4*, 396.
[176] L. Wesemann, T. J. Davis, A. Roberts, *Appl. Phys. Rev.* **2021**, *8*, 031309.
[177] H. Kwon, A. Cordaro, D. Sounas, A. Polman, A. Alù, *ACS Photonics* **2020**, *7*, 1799.
[178] Y. Zhou, H. Zheng, I. I. Kravchenko, J. Valentine, *Nat. Photonics* **2020**, *14*, 316.
[179] J. Liao, H. Shao, Y. Zhang, Y. Yan, J. Zeng, C. Lan, B. Gao, D. Chen, Q. Quan, P. Xie, Y. Meng, J. C. Ho, *Adv. Mater.* **2025**, *37*, 2419653.
[180] J. Shabanpour, S. Beyraghi, A. Cheldavi, *Sci. Rep.* **2020**, *10*, 8950.
[181] J. Zhang, J. Lou, Z. Wang, J. Liang, X. Zhao, Y. Huang, C. Chang, G. Hu, *Adv. Mater.* **2025**, *37*, 2410671.
[182] P. Prabhathan, K. V. Sreekanth, J. Teng, J. H. Ko, Y. J. Yoo, H.-H. Jeong, Y. Lee, S. Zhang, T. Cao, C.-C. Popescu, B. Mills, T. Gu, Z. Fang, R. Chen, H. Tong, Y. Wang, Q. He, Y. Lu, Z. Liu, H. Yu, A. Mandal, Y. Cui, A. S. Ansari, V. Bhingardive, M. Kang, C. K. Lai, M. Merklein, M. J. Müller, Y. M. Song, Z. Tian, et al., *iScience* **2023**, *26*, 107946.
[183] S. Zhang, X. Chen, K. Liu, H. Li, Y. Lang, J. Han, Q. Wang, Y. Lu, J. Dai, T. Cao, Z. Tian, *iScience* **2022**, *25*, 104866.
[184] Q. He, Z. Liu, Y. Lu, G. Ban, H. Tong, Y. Wang, X. Miao, *iScience* **2022**, *25*, 104375.
[185] T. Zhen, S. Zhang, X. Chen, H. Li, Y. Xu, X. Jiang, Y. Xu, Q. Wang, T. Cao, *Photonics Res.* **2022**, *10*, 1731.
[186] M. Cotrufo, S. B. Sulejman, L. Wesemann, M. A. Rahman, M. Bhaskaran, A. Roberts, A. Alù, *Nat. Commun.* **2024**, *15*, 4483.
[187] J. Zhang, J. Lou, Z. Wang, J. Liang, X. Zhao, Y. Huang, C. Chang, G. Hu, *Adv. Mater.* **2025**, *37*, 2570052.
[188] X. Wu, Z. Zhang, Z. Li, J. Zhang, X. Wang, W. Zhu, *Mater. Today Electron* **2025**, *12*, 100142.
[189] S. Peng, A. Song, Y. Bai, C. Sun, Y. Xiang, *Appl. Acoust.* **2025**, *235*, 110658.
[190] Y. Dai, C. Chen, P. Gao, X. Lu, J. Zhao, Y. Wan, X. Wang, S. Zhao, H. Liu, *Opt. Laser Technol.* **2024**, *169*, 109951.
[191] P. P. Iyer, R. A. DeCrescent, Y. Mohtashami, G. Lheureux, N. A. Butakov, A. Alhassan, C. Weisbuch, S. Nakamura, S. P. DenBaars, J. A. Schuller, *Nat. Photonics* **2020**, *14*, 543.
[192] S. T. Ha, Y. H. Fu, N. K. Emani, Z. Pan, R. M. Bakker, R. Paniagua-Domínguez, A. I. Kuznetsov, *Nat. Nanotechnol.* **2018**, *13*, 1042.
[193] Y. Luo, M. Gao, C. Lu, J. Zhang, J. Liu, Y. Tan, T. Wen, Y. Lin, *ACS Appl. Opt. Mater.* **2025**, *3*, 789.
[194] F. Wu, S. Yu, Y. He, Z. Gao, T. Zhao, *Phys. Scr.* **2025**, *100*, 045504.
[195] T. Yan, T. Guo, J. Yang, *Sci. Rep* **2025**, *15*, 9877.
[196] C. Liu, Q. Ma, Z. J. Luo, Q. R. Hong, Q. Xiao, H. C. Zhang, L. Miao, W. M. Yu, Q. Cheng, L. Li, T. J. Cui, *Nat. Electron.* **2022**, *5*, 113.
[197] Z. Jin, J. Lou, F. Shu, Z. Hong, C.-W. Qiu, *Research* **2025**, *8*, 0562.
[198] M. L. Tseng, Y. Jahani, A. Leitis, H. Altug, *ACS Photonics* **2021**, *8*, 47.
[199] W. Zhang, J. Lin, Z. Yuan, Y. Lin, W. Shang, L. K. Chin, M. Zhang, *Biosensors* **2024**, *14*, 3.
[200] Y.-C. Liu, S. Ansaryan, J. Tan, N. Broguiere, L. F. Lorenzo-Martín, K. Homicsko, G. Coukos, M. P. Lütolf, H. Altug, *Adv. Sci.* **2024**, *11*, 2401539.
[201] Z. Ren, J. Xu, J. Liu, B. Li, C. Zhou, Z. Sheng, *ACS Appl. Mater. Interfaces* **2022**, *14*, 26923.
[202] C. Liu, J. Yin, S. Zhang, *Infrared Phys. Technol.* **2021**, *119*, 103939.
[203] B. Cao, Y. Li, X. Liu, H. Fei, M. Zhang, Y. Yang, *Appl. Opt.* **2020**, *59*, 8111.
[204] L. Liu, L. Kang, T. S. Mayer, D. H. Werner, *Nat. Commun.* **2016**, *7*, 13236.
[205] M. Zhong, *Sci. Rep.* **2020**, *10*, 19845.
[206] B. Akyurek, A. Noori, Y. Demirhan, L. Ozyuzer, K. Guven, H. Altan, G. Aygun, *J. Infrared Millim. Terahertz Waves* **2024**, *46*, 5.
[207] Y. Liao, Y. Fan, D. Lei, *Nanophotonics* **2024**, *13*, 1109.

Bowen Li is currently a postdoc at the State Key Laboratory of Terahertz and Millimeter Waves, City University of Hong Kong, China, under the supervision of Prof. Johnny Ho. He received his Ph.D. in physics from the University of Science and Technology of China in 2022. His current research interests focus on the phase-change metamaterials and their THz applications.

Jiachi Liao is currently a research assistant at the Department of Materials Science and Engineering, City University of Hong Kong, China, under the supervision of Prof. Johnny Ho. He received his Materials Science and Engineering postgraduate degree from City University of Hong Kong in 2024. His current research interests focus on THz devices and metamaterials.

Di Yin is currently a Ph.D. candidate in the Department of Materials Science and Engineering at City University of Hong Kong. She earned a B.S. degree from Jiangsu University in 2017 and an M.S. degree from East China University of Science and Technology in 2020. Her research interests focus on the design and synthesis of nanomaterials for environmental pollutant removal and THz modulation.

He Shao is a postdoctoral fellow in Materials Science and Engineering at the City University of Hong Kong. She obtained her B.S. from the College of Physics, Jilin Normal University, in 2016. In 2021, she obtained her Ph.D. from Jilin University. Her research interests focus on phototransistors, memristors, and synaptic devices.

Shuai Zhang is currently a postdoc at the Department of Materials Science and Engineering, City University of Hong Kong, China, under the supervision of Prof. Johnny Ho. He received his Ph.D. from Shanghai Jiao Tong University in 2024. His current research interests focus on photothermoelectric conversion, radiative cooling, and sensors.

Baojie Chen is currently an engineer at the State Key Laboratory of Terahertz and Millimeter Waves, CityUHK. He received the B.S. and M.S. degrees in materials science from Dalian Polytechnic University, Dalian, China, in 2007 and 2010, respectively, and the Ph.D. degree in electrical engineering from City University of Hong Kong, China, in 2014. His research interests focus on optical amplifiers and the micro/nano fabrication of THz devices and components.

Chi Hou Chan is a chair professor at the Department of Electronic Engineering, City University of Hong Kong, China. He is also the director of the State Key Laboratory of Terahertz and Millimeter Waves at CityUHK. He received his Ph.D. from the University of Illinois at Urbana-Champaign, USA, in 1987. Before joining CityU in 1996, he was a tenured Associate Professor in the Electrical Engineering Department at the University of Washington. His research group focuses on computational electromagnetics, antennas, microwave and millimeter-wave components and subsystems, and terahertz science and technology.

Johnny C. Ho is a chair professor at the Department of Materials Science and Engineering, City University of Hong Kong, China. He received his Ph.D. in Materials Science and Engineering from the University of California, Berkeley, USA, in 2009. After postdoctoral training at Lawrence Livermore National Laboratory in California, he has been with the City University of Hong Kong since 2010. His research group explores novel nano-materials and nano-engineering techniques for various technological applications, including electronics, energy-harvesting, photonics, and sensors.